3D local earthquake tomography of the Ecuadorian margin in the source area of the 2016 Mw 7.8 Pedernales earthquake

Sergio León-Ríos[1,1], Lidong Bie[2,2], Hans Agurto-Detzel[3,3], Andreas Rietbrock[4,4], Audrey Galve[5,5], Alexandra Patricia Alvarado[6,6], Susan L. Beck[7,7], Philippe Charvis[8,8], Yvonne Font[9,9], Silvana Hidalgo[10,10], Mariah C. Hoskins[11,11], Laigle Mireille[12,12], Davide Oregioni[5,5], Anne S. Meltzer[11,11], Mario Calixto Ruiz[13,13], and Jack Woollam[1,1]

[1]Karlsruhe Institute of Technology
[2]Karlsruhe Insitute of Technology
[3]Université Côte d'Azur, Geoazur
[4]University of Karlsruhe
[5]Université de Nice Sophia-Antipolis, IRD, CNRS, Observatoire de la Côte d'Azur, Géoazur
[6]IG-EPN
[7]Geophysics, U. of Arizona
[8]Institut de Recherche pour le Développement
[9]UMR GeoAzur - Nice - France
[10]Instituto Geofísico-Escuela Politécnica Nacional
[11]Lehigh University
[12]Geoazur CNRS-UMR 6526
[13]Escuela Politecnica Nacional

November 30, 2022

Abstract

Based on manually analyzed waveforms recorded by the permanent Ecuadorian network and our large aftershock deployment installed after the Pedernales earthquake, we derive three-dimensional Vp and Vp/Vs structures and earthquake locations for central coastal Ecuador using local earthquake tomography. Images highlight the features in the subducting and overriding plates down to 35 km depth. Vp anomalies (˜4.5 – 7.5 km/s) show the roughness of the incoming oceanic crust (OC). Vp/Vs varies from ˜1.75 to ˜1.94, averaging a value of 1.82 consistent with terranes of oceanic nature. We identify a low Vp (˜5.5 km/s) region extending along strike, in the marine forearc. To the North, we relate this low Vp and Vp/Vs (<1.80) region to a subducted seamount that might be part of the Carnegie Ridge (CR). To the South, the low Vp region is associated with high Vp/Vs (>1.85) which we interpret as deeply fractured, probably hydrated OC caused by the CR being subducted. These features play an important role in controlling the seismic behavior of the margin. While subducted seamounts might contribute to the nucleation of intermediate megathrust earthquakes in the northern segment, the CR seems to be the main feature controlling the seismicity in the region by promoting creeping and slow slip events (SSE) offshore that can be linked to the updip limit of large megathrust earthquakes in the northern segment and the absence of them in the southern region over the instrumental period.

3D local earthquake tomography of the Ecuadorian margin in the source area of the 2016 Mw 7.8 Pedernales earthquake

Sergio León-Ríos*, *Karlsruhe Institute of Technology, Geophysical Institute, Karlsruhe, 76187, Germany*
https://orcid.org/0000-0002-6076-6388
Lidong Bie, *Karlsruhe Institute of Technology, Geophysical Institute, Karlsruhe, 76187, Germany*
https://orcid.org/0000-0002-8130-7084
Hans Agurto-Detzel, *Université Côte d'Azur, IRD, CNRS, Observatoire de la Côte d'Azur, Géoazur, 06304, Nice, France*
https://orcid.org/0000-0003-0390-9917
Andreas Rietbrock, *Karlsruhe Institute of Technology, Geophysical Institute, Karlsruhe, 76187, Germany*
Audrey Galve, *Université Côte d'Azur, CNRS, Observatoire de la Côte d'Azur, IRD, Géoazur, 06304, Nice, France*
Alexandra Alvarado, *Instituto Geofisico, Escuela Politécnica Nacional, Quito, 170525, Ecuador*
Susan Beck, *Department of Geosciences, University of Arizona, Tucson, AZ 95721, USA*
Philippe Charvis, *Université Côte d'Azur, IRD, CNRS, Observatoire de la Côte d'Azur, Géoazur, 06304, Nice, France*
https://orcid.org/0000-0003-4397-7842
Yvonne Font, *Université Côte d'Azur, CNRS, Observatoire de la Côte d'Azur, IRD, Géoazur, 06304, Nice, France*
Silvana Hidalgo, *Instituto Geofisico, Escuela Politécnica Nacional, Quito, 170525, Ecuador*
Mariah Hoskins, *Department of Earth and Environmental Sciences, Lehigh University, Bethlehem, PA 18015, USA*
Mireille Laigle, *Université Côte d'Azur, CNRS, Observatoire de la Côte d'Azur, IRD, Géoazur, 06304, Nice, France*
Davide Oregioni, *Université Côte d'Azur, CNRS, Observatoire de la Côte d'Azur, IRD, Géoazur, 06304, Nice, France*
Anne Meltzer, *Department of Earth and Environmental Sciences, Lehigh University, Bethlehem, PA 18015, USA*
https://orcid.org/0000-0002-3141-6071
Mario Ruiz, *Instituto Geofisico, Escuela Politécnica Nacional, Quito, 170525, Ecuador*
Jack Woollam, *Karlsruhe Institute of Technology, Geophysical Institute, Karlsruhe, 76187, Germany*

* corresponding author:
Sergio León-Ríos, ***sergio.leon-rios@kit.edu***

KEY POINTS

- 3D Vp and Vp/Vs models were calculated using local earthquake tomography in the region affected by the 2016 Pedernales, Ecuador earthquake
- Tomographic images highlight the heterogeneities of the margin affected by seamounts and ridges comprising the oceanic crust
- Carnegie Ridge seems the main feature controlling the seismic activity and the offshore extent of large megathrust earthquakes in the region

ABSTRACT

Based on manually analyzed waveforms recorded by the permanent Ecuadorian network and our large aftershock deployment installed after the Pedernales earthquake, we derive three-dimensional Vp and Vp/Vs structures and earthquake locations for central coastal Ecuador using local earthquake tomography. Images highlight the features in the subducting and overriding plates down to 35 km depth. Vp anomalies (~4.5 – 7.5 km/s) show the roughness of the incoming oceanic crust (OC). Vp/Vs varies from ~1.75 to ~1.94, averaging a value of 1.82 consistent with terranes of oceanic nature. We identify a low Vp (~5.5 km/s) region extending along strike, in the marine forearc. To the North, we relate this low Vp and Vp/Vs (<1.80) region to a subducted seamount that might be part of the Carnegie Ridge (CR). To the South, the low Vp region is associated with high Vp/Vs (>1.85) which we interpret as deeply fractured, probably hydrated OC caused by the CR being subducted. These features play an important role in controlling the seismic behavior of the margin. While subducted seamounts might contribute to the nucleation of intermediate megathrust earthquakes in the northern segment, the CR seems to be the main feature controlling the seismicity in the region by promoting creeping and slow slip events (SSE) offshore that can be linked to the updip limit of large megathrust earthquakes in the northern segment and the absence of them in the southern region over the instrumental period.

PLAIN LANGUAGE SUMMARY

Using seismic data recorded by the permanent Ecuador network and the large emergency installation after the 2016 Pedernales earthquake, we obtained the velocity structure together with precise earthquake locations for the coastal Ecuadorian margin. Our images highlight the heterogeneities of the subduction zone affected by seamounts and ridges comprising the oceanic crust. These features

play an important role in controlling the seismic behavior of the margin. While seamounts can contribute to the occurrence of intermediate (M~7-7.5) megathrust earthquakes in the north, the Carnegie Ridge seems to be the main feature controlling the seismicity in the region by promoting creeping and slow slip events offshore that can be linked to the updip limit of large megathrust earthquakes in the northern segment and the absence of them in the southern region.

1. INTRODUCTION

The subduction margin of Ecuador presents a structural segmentation along strike mainly caused by subducting topography coming from the oceanic plate (e.g. Collot et al., 2002; Gailler et al., 2007; Marcaillou et al., 2016). Additionally, the margin hosts a wide variety of seismic behavior including large megathrust earthquakes, seismic swarms, repeating earthquakes and slow slip events (SSE, e.g. Font et al., 2013; Rolandone et al., 2018; Agurto-Detzel et al., 2019). To the north of the equator, the margin has produced several large magnitude ≤ 7.5 subduction earthquakes in the past (Ramirez, 1968; Kelleher, 1972; Abe, 1979; Herd et al., 1981; Kanamori and McNally, 1982; Mendoza and Dewey, 1984; Beck and Ruff, 1984; Swenson and Beck, 1996). South of the equator, just a small number of large subduction earthquakes have been observed (Egred, 1968; Dorbath et al., 1990; Bilek et al., 2010), with only two Mw > 7.0 events that occurred close to Bahia Caraquez (Storchak et al., 2013), and seismic activity mostly associated with swarms (Segovia, 2001; Segovia, 2009; Vaca et al., 2009), repeating earthquakes (Rolandone et al., 2018) and SSE (Mothes et al., 2013; Vallee et al., 2013; Chlieh et al., 2014; Collot et al., 2017; Segovia et al., 2018; Vaca et al., 2018; Rolandone et al., 2018). The Mw 7.8 Pedernales earthquake occurred in 2016 and was located in a region previously identified as highly coupled by Chlieh et al. (2014). Nocquet et al. (2017) showed that an area of about 100 x 40 km2 was affected by coseismic slip (see Figure 1a). The associated after-slip was described by Rolandone et al. (2018) highlighting that areas surrounding the mainshock experienced post-seismic slip and SSE. This phenomenon, where several types of slip behavior are capable of coexisting during inter-, co- and post -seismic stages suggests a highly heterogeneous plate boundary.

Although the Ecuadorian margin has been widely studied, there is still no consensus about a regional scale 3D velocity model, especially for the coastal area and the marine forerarc, where megathrust earthquakes exert great seismic hazard. Previous local studies in the Esmeraldas segment (Gailler et al., 2007; Agudelo et al., 2009; Garcia-Cano et al., 2014), La Plata island (Gailler et al., 2007) and part of the Carnegie Ridge (CR) (Sallares and Charvis, 2003; Sallares et al. 2005; Graindorge et al., 2004 and Gailler et al. 2007) have contributed to our understanding of the first order characteristics of the physical properties in the margin. On a regional scale, Font et al. (2013) built a velocity model for the forearc by combining geodynamic, structural and velocity data, reproducing the slab geometry. Araujo et al. (2016) derived a seismic velocity model and Moho depth for a larger area based on seismic data from the Ecuadorian permanent network (RENSIG), however small-scale structures (e.g. seamounts) that could impact the seismic behavior in the forearc region were not resolved. Lynner et al. (2020) and Koch et al. (2020) used ambient noise and a joint ambient noise and receiver function methods respectively to image the coastal forearc but were unable to image the marine forearc.

Based on the aftershock activity of the 16th April, 2016 Pedernales earthquake, recorded by our temporary seismic network which included ocean bottom seismometers (OBS) installed along the trench axis (Leon-Rios et al., 2019; Meltzer et al., 2019), we derive a novel three-dimensional velocity model for Vp and Vp/Vs together with precise hypocentral locations for the central coastal area of Ecuador. Local earthquake tomography imaged the physical properties that were then incorporated into the regional seismotectonic and geological setting to provide a descriptive interpretation of the major features involved in the Ecuadorian subduction process. Our findings highlight a very heterogeneous margin with seamounts and large bathymetric features within the oceanic crust, but also an overriding plate highly affected by large-scale faults. Finally, we discuss how these structures might contribute to controlling the seismic activity in the Ecuadorian margin.

2. TECTONIC SETTING

The Ecuadorian margin is controlled by the subduction of the oceanic Nazca plate beneath the continental South American plate. This process occurs with an east–west convergence rate of ~47 mm/yr (Trenkamp et al., 2002; Kendrick et al., 2003; Nocquet et al., 2009, Nocquet et al., 2017). The margin has been recognized as highly segmented and mainly erosional (Collot et al., 2002; Gailler et al., 2007; Marcaillou et al., 2016). The continental forearc is divided by the Chingual-Cosanga-Pallatanga-Puna (CCPP) fault zone (Alvarado et al., 2016), limiting the North Andean Sliver (NAS) as shown in Figure 1a. In front of the NAS, the Nazca Plate is less than 26 Ma old (Lonsdale, 2005) and subducts at a relative rate of about 46 mm/yr (Chlieh et al., 2014).

Offshore, the study area is characterized by the presence of large bathymetric features such as the aseismic CR, the Atacames seamount chain and, farther north, the Yaquina graben interpreted as an extinct rift and transform fault closer to the trench (Lonsdale et al., 2005; Hardy et al., 1991) (see Figure 1b). These significant along-strike and along-dip structural variations which might exist at greater depth on the subducted portion of the plate may contribute to the diverse patterns of seismicity along strike (Gailler et al., 2007; Font et al., 2013; Agurto-Detzel et al., 2019). The CR subducts beneath the Ecuadorian trench between latitude ~1°N and ~2°S (see Figure 1). It is ~280 km wide and 2 km high and is currently subducting in ENE direction. Residual bathymetry (Figure 1b) derived by Agurto-Detzel et al. (2019) images the rough topography caused by the CR. The CR was formed by the Galapagos hot-spot (GHS) located about 1000 km west of the coastline of Ecuador. At the northern flank of the CR, a series of seamounts including the Atacames seamounts are subducting beneath the South American plate. Marcaillou et al. (2016) points out that the Atacames seamounts play an important role in the nucleation of large subduction earthquakes. The thickness of the oceanic crust varies along strike–from 5 km in the north, close to Esmeraldas (~1°N), to 14 km in the south (~1°S), reaching its maximum of 19 km beneath the crest of the CR (Meissnar et al., 1976; Calahorrano, 2001; Sallares and Charvis, 2003; Sallares et al., 2005; Graindorge et al., 2004; Garcia-Cano et al., 2014).

Toward the coast, the current forearc in central Ecuador is the result of subsequent accretion of lithospheric material and arc rocks that occurred between the late Cretaceous to the Paleocene/Eocene (Reynaud et al., 1999; Jaillard et al., 2009). A thin layer of sediments of 500 m to 1000 m (Jaillard et al., 2000) covers most of the forearc. Distributed along the coastline, magmatic outcrops have been associated with the Piñon formation (Reynaud et al., 1999; Luzieux et al., 2006; Reyes and Michaud, 2012) which is identified as “the Cretaceous igneous basement of western Ecuador” (Reynaud et al., 1999) and extends along the whole study area up to the CCPP fault to the east. In the Manta area, the San Lorenzo block, a mix of volcanic conglomerates, appears in conformity with the Piñon formation (Reynaud et al., 1999; Reyes and Michaud, 2012) creating oceanic terranes. Quaternary sediments cover these as well as other small formations forming several basins along the coast such as the Borbon, Manta-Jama and Manabi basin (see (1), (2) and (3) in Figure 1b). The local tectonic and seismic activity is controlled by major faults (Reynaud et al., 1999; Luzieux et al., 2006; Reyes and Michaud, 2012, Font et al., 2013; Agurto-Detzel et al., 2019; Leon-Rios et al., 2019; Soto-Cordero et al., 2020). Reyes and Michaud (2012) updated the coastal geological map for Ecuador extending several faults observed at the surface. The main geological structures and faults (Figure 1b), contribute to regional tectonic control but also allow the circulation of fluids within the margin.

3. NETWORK AND DATASET

3.1 The seismic aftershock network

After the 2016 Pedernales mainshock, a large international collaboration coordinated a rapid response to install a temporary seismic network (Meltzer et al., 2019). One month after the mainshock, a dense temporary amphibious network was deployed comprising broadband and short period seismic land stations and OBS stations along the trench. Figure 1b shows the spatial distribution of the final deployment including both temporary and permanent deployments consisting of more than 80 stations with a station spacing of approximately 10 – 30 km. Onshore stations were fully operative from May 2016 to June 2017. Offshore, OBSs were recording between mid-May and November in 2016.

3.2 Dataset

To extend the catalogue prepared to obtain the 1D velocity model (Leon-Rios et al., 2019), we incorporated more events from the refined aftershock catalogue by Agurto-Detzel et al. (2019). Seismicity with $M_L > 2.5$, recorded between May and November 2016, and located in the vicinity (300 x 200 km2) of the temporary network was included in the 3D inversion process. From this catalogue, P- and S-wave arrival times were manually picked using the Seismic Data Explorer (SDX) software package (http://doree.esc.liv.ac.uk:8080/sdx) that utilizes a modified hypo71 algorithm for the hypocenter location (Lee et al., 1972). Following the procedures from Agurto et al. (2012), Hicks et al. (2014) and Leon-Rios et. (2019) we assigned pick error categories, referred as weights, from 0 to 4 to describe the quality of the selected arrival times. Each weight corresponds to the following time uncertainties: Weight 0 (< 0.04 s); Weight 1 (0.04 – 0.1 s); Weight 2 (0.1 – 0.2 s); Weight 3 (0.2 – 1 s); Weight 4 (> 1 s). Events were located using the minimum 1D model and station correction terms from Leon-Rios et al., (2019). Finally, aftershocks with at least 10 P and 5 S observations and azimuthal gap < 230° were included in the catalogue to get a total of 568 earthquakes containing 10628 P-phases and 9134 S-phases.

4. METHOD: LOCAL EARTHQUAKE TOMOGRAPHY

Following the procedure detailed by Husen et al. (2000), Haberland et al. (2009) and Hicks et al. (2014), we performed a series of iterative travel time inversions to obtain Vp, Vp/Vs and hypocentral locations using SIMULPS (Thurber, 1983, 1993; Eberhart-Phillips, 1990; Evans et al., 1994). To compute the velocity and hypocentral solutions, this algorithm performs iterative travel time inversions within a 3D nodal grid defined by the user. For our inversion, we defined a total volume of 1480 x 1200 x 350 km3 and a fine grid in our area of interest of 200 x 250 x 60 km3 (see Figure S1) with several nodes organized perpendicular and parallel to trench axis (x and y respectively) and in the z component. Grid nodes were added following a staggered approach increasing the complexity of the calculations from our reference 1D velocity model to the final 3D model.

For all the stages, Vp velocity was calculated initially and then used as input to perform the Vp/Vs inversion. First, we extended our minimum 1D velocity model (Leon-Rios et al., 2019) to a 2D plane oriented perpendicular to the trench. Then, we performed first order calculations to define the best damping value. After the Vp inversion, we fixed the P-phase velocity and inverted for Vp/Vs. Events on each segment were used to calculate damping curves and subsequent inversion. Also, we applied a smoothing technique to improve our lateral resolution (Haberland et al. 2009, Collings et al. 2012; Hicks et al. 2014). Due to the segmentation along the margin and to get robust hypocentral solutions, we separated the inversion into north and south segments, using a line in between P5 and P6 (Figure 1) as the dividing line.

Finally, the precise hypocentral locations and their corresponding arrival times resulting from the 2D inversions, were subsequently inverted using a smooth 2D initial model projected over a finer grid to increase resolution along strike (see Figure S1). Here, a damping curve was also calculated to obtain our final 3D velocity model. A detailed description of each step is given in the following sections.

4.1. Two-dimensional modeling

To obtain the 2D velocity model (2DVM), we extended our minimum 1D model (Leon-Rios et al., 2019) in a 2D grid with a minimum lateral spacing of 15 km to resolve velocity structure in west-east direction. In depth, we used the layers of the reference 1D model to set the nodes separation. Distance between nodes varies from 2.5 km at shallower layers to 10 km at greater depths (see Figure S1). To have a better constraint of the area, with a seismicity better distributed and a large amount of P- and S-onsets, we augmented the number of events in the 1D catalogue (Leon-Rios et al., 2019) from 227 to 549 (see Table 1). The structural differences between areas located north and south of the equator forced us to split the calculation in two sections to obtain robust earthquake locations in this initial stage. For the inversion to the north (2D-N), we used 317 events with 5479 P- and 4559 S-onset phases (see Table 1). For the south section (2D-S), a total of 232 aftershocks containing 4821 P- and 4128 S- onset phases were used. Several damping values were tested, as described in Eberhart-Phillips (1990), to select the best one to perform the inversions (see Figure S2). A rough 2D model was calculated and used as input for the following inversions. For both north and south sections, we applied a smoothing technique (Haberland et al. 2009, Collings et al. 2012 and Hicks et al. 2014) by shifting nodes by a third of the minimum spacing to improve our lateral resolution. The resulting averaged Vp model was used as the new starting model to invert for Vp/Vs.

		# events	P-phases	S-phases	Total phases	Damping		Model VAR		Localization VAR		RMS	
						Vp	Vp/Vs	Vp	Vp/Vs	Vp	Vp/Vs	Vp	Vp/Vs
1D*		227	4939	3931	8870	-	-	-	-	-	-	0.33	0.30
2D	North	317	5479	4559	10038	500	800	0.1959	0.2080	0.08	0.09	0.28	0.31
	South	232	4821	4128	8949	500	2000	0.2002	0.1705	0.09	0.08	0.30	0.28
3D	-	568	10628	9134	19762	500	600	0.2160	0.2148	0.10	0.09	0.29	0.30

Table1. Summary of number of events, P-and S-phases, damping values and variance for the model and the relocated aftershocks for each step towards the three-dimensional model calculation. (*) As the 1D model (Leon-Rios et al., 2019) was obtained using a different program, damping values were not included.

4.2. Three-dimensional modeling

Using the results from the previous stage, we continued to calculate a 3D velocity model (3DVM). At this stage, we added 19 more events (Ml > 2.5 and gap < 230°) that filled blank spaces left in the 2D modeling, helping us better constrain the models in N-S direction. In total, we inverted 568 aftershocks with 10628 P- and 9134 S-phases (see Table 1). Also, we included more nodes along W-E trench perpendicular profiles along strike to increase resolution in that direction. The profiles and node distribution for this stage are shown in Figure 1b and Figure S1, respectively. The grid for the 3D inversion comprises 11 profiles distributed in a volume with a minimum spacing, of 15 km, 20 km and 2.5 km, for the x (east), y (north) and z (down) axis, respectively.

With this setting, we incorporated 2D-N and 2D-S arrival times and inverted over a smooth 2D initial model, shown in Figure 4, which was extended in the described 3D grid. We used such a 2D starting model to avoid along strike smearing, but also perform the inversion for a combined North-South model as a reference and check the robustness for the inversion due to different starting models. Following the same procedure conducted for the 2D modeling, we calculated damping curves (see Figure S2) and inverted first for Vp and subsequently for Vp/Vs.

5. Resolution

Although the setting of our amphibious experiment ensures a good coverage for recording the aftershocks, the irregular distribution of both stations and earthquakes raises the problem of resolution heterogeneity within the 3D volume. To identify areas that are well resolved and to distinguish them for areas that are poorly resolved, we inspected critical parameters from the model resolution matrix and also conducted checkerboard tests. Finally, to estimate the standard deviation and analyze the restoring capability of our 3D model, we performed bootstrap and synthetic recovery tests.

5.1. Model resolution matrix (MRM)

We investigated in detail the MRM to provide insights on how well resolved the model parameters (seismic velocities) are. By taking the ratio between off-diagonal and diagonal elements of the MRM, we derived the spread function (SF, Toomey and Foulger, 1989) helping to identify areas with good and poor ray coverage. We also inspected the size and orientation of smearing by contouring the 70%

value of the diagonal elements at each row of the MRM (eg. Haberland et al., 2009; Collings et al., 2012; Hicks et al., 2014). In general, large diagonal elements of the MRM, small SF and rounded 70% contour lines around the grid nodes are related to well resolved areas.

Cross sections in Figure 2 and 3 show the resolution of our 2DVM and 3DVM for both Vp and Vp/Vs. We consider well recovered areas when SF < 65% of its maximum value (eg. Haberland et al., 2009; Hicks et al., 2014). 2DVM show a well resolved Vp in both, north and south segments. The Vp/Vs ratios show a less constrained area, mainly because of a lower number of S-phase onsets. For our 3DVM, Figure 3 shows a representative sample of the MRM (Figure S3 presents the resolution obtained for all profiles). From north to south, we observed how the central profiles are better resolved. At ~1°N, in profile 1, the lack of seismicity and data from OBS at this latitude confines the resolution contour to an area with data coming from a seismic cluster in the upper crust. In contrast, the rest of the profiles show wider resolution contours. In terms of MRM, the small SF and rounded-like shape of the 70% resolution kernels indicate well resolved areas. Although some areas in the marine forearc can show lateral smearing (P5-P6, see Figure S3), it is important to highlight how the resolved areas were increased trenchward thanks to the presence of the OBS distributed offshore. The portion of the marine forearc devoid of OBSs (P1) is not resolved at shallow depths (<5-7 km). To the east, we observe areas with sub-vertical smearing indicating lack of horizontal ray paths. This occurred mainly due to the location of the sources. For Vp/vs (Figure 3), the resolution contours are smaller due to the number of S-phases detected, we were able to resolve the central part in all of them. In terms of smearing, we see a transition in the shape of the 70% resolution kernels that goes from small in the central part (around 0 km in the x-axis) to large-elongated shape near the edges limiting the resolution in these areas (see Figure S3).

5.2 Checkerboard test

To analyze the resolution capability of our data set we evaluate synthetic reconstruction tests. A classic tool to explore this matter is by performing a checkerboard test (Spakman et al. 1988). This type of analysis helps us to estimate how well resolved are different sizes of anomalies in our model and how well amplitudes are recovered. Synthetic travel times were calculated using the observations from our final 3D inversion over an alternating pattern of positive and negative anomalies of 5% of the inverted model. Different sizes of anomalies (15 km and 30 km) were tested. Then, the inversion method was applied to recover the original structure. Finally, we evaluated the agreements (dv) between the anomalies in the initial and final models to assess the resolution capability of our dataset. Anomalies of 30 km wide (Figure 4 and S4) show well recovered velocities (dv ~5%) down to ~40 km depth. Lateral and vertical extension of the recovered anomalies show a recovery < 2% deeper and on the edges of the profiles. For smaller perturbations (15 km), areas of good recovery are similar to those from larger anomalies, showing a reduction of recovered velocities (dv < 2%) when deeper than ~ 30km. We observe a reduction in the recovering capacity in P1 where the lack of seismicity limits the resolution only to a small region at shallower depths (<20 km) below the coastline. P2 shows a good recovery reaching dv ~4% in its central region although the edges still show the effects of reduced seismicity. Profiles P4-P8 are well recovered (dv ~5%) in the central areas, reaching good resolution up to the trench. Finally, the southernmost profile P10 also shows well recovered areas although the reduced seismicity in that region reduces the in-depth restoring capacity to <2% down to 20 km.

5.3 Synthetic recovery test

We also performed characteristic model restoring tests to assess the imaging properties of our obtained 3D velocity model. We focused on the analysis of a subducting seamount shaped with a low Vp anomaly and located close to the trench in profiles P4 and P5. The synthetic model also included a low Vp feature at ~20 km depth, located in P7 (see Figure 4c and Figure S5). Synthetic travel times were computed as described above and subsequently inverted over the 2D initial model. Profiles where the low Vp anomalies were included recovered similar shapes and values. We observe that P4 is more likely to recover the low Vp by getting values ~5 km/s down to 5 km depth. P5 restored the reduced velocities (~5.5 km/s) although the Vp=5 km/s show only a small size down to 2.5 km depth. In terms of the low Vp anomaly at ~20 km depth in profile P7, the model can recover the anomaly although with a reduced amplitude. Figure 4c shows profiles P4 and P7 for this test while Figure S5 presents the recovered velocities for the central profiles (P3-P8).

To check the influence of the initial model on our obtained Vp velocities, especially for the slab crust at depth > 30 km, we conducted a second synthetic test based on the 2D-N Vp model. The 2D-N model, with a low Vp feature near the trench and without plunging slab crust deeper than the upper plate's Moho, was projected along all grid nodes and synthetic arrival times were calculated. Similar to the previous test, arrival times were subsequently inverted over a smooth initial model (see Figure S6). In general, the recovered velocities agree with the initial 2D-N model, with major features present in almost all profiles. However, this test highlights the structural segmentation of the margin by showing how the restored model varies as we move south. Close to the trench we observe how the low Vp anomaly disappears in P5-P6, then reappears in P7 and P8 but with a broader and deeper extension.

To further analyze possible artifacts and check the robustness for our final model, we computed a 3D inversion based on an initial model formed by the merged 2D-N and 2D-S models. The inversion followed the same procedure described for our staggered 3D inversion. Results for this inversion are shown in Figure S7 and S8, to be compared to figure 6 and 7, respectively. In general, the velocities imaged by the merged 2D-N and 2D-S models are similar to those obtained by the smooth initial model. Main features at the surface are well resolved, however, along strike smearing is observed, especially for the features close to the trench. This suggests that the merged modeling strategy can add possible artifacts to the inversion and confirms the robustness of our 3D model based on high quality arrival times inverted over a smooth initial 2D model.

5.4 Bootstrap

A last sensitivity test was performed to estimate a first order standard deviation for the obtained velocities. We conducted a bootstrap test by creating a subset of data comprising 80% of the actual catalogue which was subsequently inverted. Aftershocks included in the tested catalogue were randomly selected and the inversion parameters were the same as described for the 3D velocity model. We repeated this process 100 times and calculated the standard deviation at each node of the grid (see Figure S8). Finally, the overall mean value was calculated to estimate the error of our obtained Vp and Vp/Vs models. Maximum estimated standard deviation for Vp is 0.27 km/s and for Vp/Vs 0.009 while mean values are 0.04 km/s and 0.004, respectively.

6. Results

The 2DVM and 3DVM highlight the main structural features for the central Ecuadorian subduction zone. Based on the inspections of both, SF and checkerboard test, we estimated regions with good resolution that, in general, extend ~130 km eastward from the trench axis. In depth, we can resolve velocities down to ~35 km. The following sections describe the results shown in Figures 5, 6 and 7. Cross sections were produced for 2DVM and 3DVM (see Figure 5 and 6, respectively). We used slab1.0 (Hayes et al., 2012) as a reference for the plate interface at depths greater than 15 km and modified the shallower part by using the trench location from Collot et al. (2005) and our obtained aftershock distribution. Also, horizontal slices for Vp and Vp/Vs were taken at 2, 5, 10 and 20 km depth to observe velocity changes in depth (Figure 7). The margin shows Vp/Vs ratios ranging from 1.74 to 1.94 in agreement with Hyndman (1979) and Christensen (1996; 2004) that suggested typical Vp/Vs values in the upper oceanic crust of 1.78 to 2.11 depending on the percentage of serpentine, fluids or lithology.

6.1. Two-dimensional velocity models

From the resulting 2DVM, we can identify first order features in both, north and south, segments. Figure 5 shows cross sections for Vp and Vp/Vs where the Vp=7.0 km/s contour images the geometry of the crustal part of the downgoing plate and a contrasted thickness of the slab crust between north and south segments.

In the downgoing plate, we also observe elevated Vp/Vs ratios (~1.90) located close to the trench. In the overriding plate, velocity anomalies correspond to major geological structures, such as basins and geologic formations distributed along the margin. North and south profiles in Figure 5 show prominent low Vp anomalies (~4 km/s) and alternated distribution of Vp/Vs ratios, with low (~1.75) and high (~1.90) values, extending eastward at shallow depths. Geologic features associated with these anomalies have been mapped at the surface by Reyes and Michaud (2012) and will be discussed later.

Finally, in terms of seismicity, we observe that most of the aftershocks are located along the slab interface. However, we observe a change from a more interface-aligned organization of aftershocks in the north to a more dispersed distribution of events in the south.

6.2. Three-dimensional velocity model

Figures 6 and 7 show our resulting Vp and Vp/Vs 3DVM together with the relocated seismicity, displayed in horizontal slices and cross sections, respectively. At shallow depths (z=2 km and 5 km, see Figure 6), we image a prominent elongated N-S feature (~30 x 150 km) along the coast, having Vp ranging from 5.0 km/s to Vp=5.5 km/s. We also observe low velocities (Vp~4.5 km/s) south and east of the high Vp anomaly, suggesting a high velocity contrast at shallow depth in the area. At the same depths (z=2 km and 5 km), high and low Vp/Vs ratio anomalies (>1.85 and <1.80) are observed at the location of the high and low Vp regions.

Cross sections in Figure 7 image in detail the subducting oceanic Nazca plate. By comparing the depth of the Vp 7.2 – 7.5 km/s iso-contour at ~20 km eastward of the trench, we observe a thick crust ~15 km which is consistent with previous observations for the Nazca plate thickness (Sallares and Charvis, 2003; Gailler et al., 2007; Cano et al., 2014). In terms of Vp/Vs ratios, we find values ~1.90 close to the trench in profiles P2-P9 (Figure 7).

Close to the trench, a prominent low Vp anomaly (~5.5 km/s) is observed in the oceanic crust. Horizontal slices at z=10 km, in Figure 6, show the along strike extension where three low Vp patches are illuminated. Moreover, a detailed inspection of the cross sections (see Figure 7), show a prominent low Vp feature of ~20 km wide in P4. Also, this low Vp anomaly shows a broader extension to the south from P5-P9. In terms of Vp/Vs, it is also possible to observe a N-S variation in the area where the low Vp anomaly is described. We image Vp/Vs ratios ~1.75 in P4-P5 that change to ~1.85 from P6-P9 close to the trench.

Finally, from the relocated aftershocks displayed in vertical and horizontal profiles, we observed a clustered distribution mainly organized along the slab interface, as described by Agurto-Detzel et al. (2019), Meltzer et al. (2019) and Soto-Cordero et al. (2020) but also at shallower depths (<20 km) in the upper crust as discussed by Leon-Rios et al. (2019) and Hoskins et al. (2018).

We found a group of seismicity in profile P1 that corresponds to the Esmeraldas activity occurred in July 2016. Cross sections in profiles P2-P5 show the seismicity mostly aligned along the slab interface at depths > 15 km. In contrast, close to the trench in P4, we observe a prominent sub-vertical organization of events showing a depth range between 5 to 10 km. Aftershocks in profile P6-P7 appear with a more disperse distribution where upper crust activity is also observed in the region. However, it is still possible to identify some clustered disposition close to the trench (~10-15 km depth). P8 shows clustered activity in the oceanic crust, located ~10-15 km east from the trench. Finally, in profiles P9 and P10, the observed seismicity is reduced significantly with few events in the slab interface, and also clustered activity in the upper crust with a vertical distribution occurring at shallower depths (~10-15 km) in P9.

7. Interpretation and Discussion

Upper plate crust (UC)

P-wave velocities in the UC can be associated with geological structures described by Reyes and Michaud (2012) and shown in Figure 1b. Observations from horizontal slices at shallow depths (z=2 and 5 km) are labeled in Figure 6 relating the high Vp (~5.5 km/s) feature to outcrops of the Piñon formation (P). The same structure is well imaged in Vp/Vs profiles P4-P6 in Figure 7. This formation is clearly imaged by relatively low Vp/Vs ratios (1.75 – 1.80) distributed along the coastline between 0.5°S and ~0.1°N, and it is part of the oceanic terranes in the overriding plate (Reynaud et al., 1999; Luzieux et al., 2006; Reyes and Michaud, 2012). We can estimate its lateral extent up to ~25 km. In contrast, at 2 km depth, we observed an elongated N-S orientated low Vp (~4.5 km/s) body that extends southward. This feature can be associated with the northern part of a sedimentary basin, namely the Manabi basin (M; Reyes and Michaud, 2012). The Manabi basin is well identified by a large scale (~80 km x 27 km) NNE high Vp/Vs (1.85 – 1.90) anomaly associated with non-consolidated and hydrated rocks. We also imaged what might be the basin depocenter by identifying a region of reduced Vp (4.5 km/s) and elevated Vp/Vs ratios (~1.85) down to 5 km depth (see Figure 6).

The Manabi basin is a large structure that extends for about 200 km along strike and its north-eastern boundary is controlled by the Jama Fault System (JFS) which separates this basin from the Cretaceous Piñon formation. The contrasted nature of these formations could be related to the high contrast imaged in the horizontal slices of both Vp and Vp/Vs models. This fact has been previously described based on station correction terms from our derived 1D velocity model (Leon-Rios et al., 2019). Moreover, Vp/Vs cross sections P4-P6 (see Figure 7) highlighted this contrast of Vp/Vs ratios, around 100 eastward from the trench, up to 5-10 km depth. Collot et al. (2004) and Michaud et al. (2015) have suggested that the JFS extends offshore forming an active flower-like fault structure in the marine forearc, however our model does not show clear evidence to support that hypothesis. Southernmost profiles P9 and P10, image reduced ratios covering a large area in the overriding plate. These anomalies can be associated with the San Lorenzo formation (SL) mapped by Reyes and Michaud (2012 – Figure 6) and also observed by Lynner et al. (2020) and Koch et al. (2020).

Iso-velocity contours of Vp~6.0 – 6.2 km/s in cross sections (Figure 7) also contribute to imaging a transition zone in the marine forearc at depth above the interplate, which separates a wide deformed, eroded and fractured trench-ward region of accreted oceanic Cretaceous rocks, with Vp~5.5 km/s, from a deeper more consolidated, less deformed and more mechanically resistant area to the east (Vp>6 km/s and depth > 7 km; Gailler et al., 2007; Cano et al., 2014). Following this iso-velocity contour (Vp~6.0 – 6.2 km/s) along the vertical sections (Figure 7), we observe that in profiles P3-P5, the transition zone is located between 50 to 60 km eastward of the trench and might be related to the west limit of the Piñon formation imaged at shallower depths by reduced Vp/Vs ratios (~1.75). As suggested by Wang and Bilek (2011) and Marcaillou et al (2016), this possible highly damaged frontal zone can prevent seismic rupture to nucleate at shallow depths on the megathrust fault. Its eastern limit of this frontal domain could indicate a major feature controlling the up-dip rupture extension of moderate-magnitude megathrust earthquakes such as the Mw 7.8 in 1942 and the Mw 7.8 in 2016 occurring on the deeper portion of the fault. Similar behavior has been proposed by Cano et al. (2014) for the northern Esmeraldas region and the Mw 7.7 earthquake in 1958 (see Figure 1a). As the ~50-60 km wide low velocity wedge is directly affected by the subducting plate and the possible frontal erosion caused by the incoming topography (Dominguez et al., 1998; von Huene et al., 2000; Sage et al., 2006), it is expected that the accreted volcanic rocks that shaped the oceanic terranes in the outermost forearc on this region are fluid-saturated, altered and disaggregated (Contreras-Reyes et al., 2012; Cano et al., 2014; Marcaillou et al., 2016). Finally, towards southern profiles (P6-P8), the described transition zone reduces its extension to less than 40 km (at ~10 km depth) leading to a margin with Vp ~6 km/s, consistent with the observations made by Gailler et al. (2007).

Subducting Oceanic Lithosphere

In general, as it is shown in Figure 7, Vp velocities resulting from our 3DVM image a predominant area of Vp ~4.5 – 7.5 km/s dipping eastward that we associated to mid oceanic ridge basalts (MORB) and basaltic lavas formed at a spreading center that comprise the oceanic crust (White et al., 1992) but also to serpentinized rocks that contribute to reduce Vp values (Marcaillou et al., 2008). Because of the inherent limitations of our dataset and model, with in-depth grid node spacing of 5 km (down to 30km depth), we cannot assess an exact value for oceanic crustal thickness. Considering the iso-velocity contour of 7.5 km/s that mimics the Moho, we have some insights on the downgoing plate characteristics. On average, we observe no significant changes in oceanic crustal thickness that appears to be around 15 km (see Figure S10). An abnormally thick oceanic crust has been previously observed by marine seismic experiments (Sallares and Charvis, 2003; Sallares et al., 2005; Gailler et al., 2007) in the area that is related to the presence of the CR. Our tomography shows similar velocities for the upper crust from previous studies (Sallares et al., 2005, Graindorge et al., 2004) and the presence of the Carnegie ridge is on all profiles where the base of the oceanic crust is resolved from P3 to P9, highlighting its extension under the margin. The CR resulted from the cooling of mantle melted material originated ~15 - 20 Myr B.P. by the interaction between the Galapagos hot-spot and the Cocos-Nazca spreading center (Lonsdale, 1978; Sallares and Charvis, 2003; Gailler et al., 2007), adding material to the lower layers of the oceanic crust and shifting the Moho location to greater depths (see z=20 km in Figure 6 and 7). Furthermore, looking at the along strike variations of the 7.5 km/s iso-velocity contour on profiles P4 to P7 (see Figure S10), the flattening of the contour at ~40 km from the trench shows a thinning of the downgoing crust that could be interpreted as the eastern border of the CR or strong variations of the CR structure (see Figure 8). If indeed we observe the eastern border of the CR, it seems to be close to the coast, not having reached it yet. This position of the eastern border of the CR is consistent with the extension of the Malpelo ridge, as both were part of the same ridge (Lonsdale, 1978). Such interpretation implies a prior process that resulted in the coastal Cordillera uplift such as stripping events at the base of the forearc crust (Ménant et al., 2020) and/or deep slab folding at depth (Cerpa et al., 2015).

In terms of Vp/Vs, we image elevated ratios of ~1.85 dipping eastward, close to the trench. This feature is intersected with Vp/Vs ratios ~1.80 related to the oceanic terranes (see profiles P3-P5 in Figure 7). We observe differences in the Vp/Vs ratios between north (P2-P5) and south (P6-P10) segments along the downgoing plate. The CR shows high Vp/Vs ratio anomaly (> 1.85) that changes to normal oceanic values when the slab reaches 10 km depth (P6-P10), associated with seismicity on P7-P9. To the north this feature seems affected by the low Vp anomaly observed on P3 and P5, and shows a low Vp/Vs value.

Elevated Vp/Vs close to the trench

Our 2DVM (see Figure 5) shows for the north and south segments elevated Vp/Vs ratio contours (>1.85), illuminating the subducting oceanic crust close to the trench. However, both profiles reach values >1.90 indicating a highly hydrated region close to the trench. More in detail, the 3DVM helps us to identify the areas where these highs in Vp/Vs ratio are located. Horizontal slices, at z=5 km, in Figure 6, show two small patches of Vp/Vs ~1.85 located at 0° and 0.5°N. Similarly, slice at z=10 km images two N-S elongated anomalies of elevated ratios (>1.85) that extend for ~50 km, in the north, and ~100 km in the south, respectively. Maximum value is reached at 0.5°N with Vp/Vs ~1.92. High Vp/Vs ratios along the trench axis have been observed along other subduction zones (e.g. northeastern Japan (Nakajima et al. 2001), central Chile (Haberland et al., 2009; Hicks et al. 2014) and Costa Rica (Bangs et al., 2015). This feature is associated with the lithology of the oceanic crust, the presence of fluids from dehydrating subducted sediments (Husen et al., 2000), and hydrated oceanic crust with extensional faults formed before subduction in the outer-rise (von Huene et al., 2004).

The central Ecuadorian subduction zone has been described as an erosive margin with a low input of sediments (Collot et al., 2002; Gailler et al., 2007; Marcaillou et al., 2016), and therefore other mechanisms explaining the elevated Vp/Vs along the trench are needed.

Cross sections P4-P5, in Figure 7, suggest a positive relation between subducting topography and elevated Vp/Vs ratios (>1.85) on the edges of these features. Moreover, the seismicity distributed with a sub-vertical disposition of ~10 km length inside the oceanic crust gives us insights about possible areas of weakness caused either by the collision of bathymetric features with the overriding plate and/or the reactivation of extensional faults on the Nazca plate, created by the outer rise bending prior subducting (von Huene et al., 1989; Von Huene et al., 2004). In Figure 8, we suggest that the high ratios imaged by our Vp/Vs model are also associated with the subduction of bathymetric features, such as the Atacames seamounts, which cause deformation and generation of weakness areas close to the trench. This process contributes to high rates of fluids migration by increasing the porosity and permeability on both plates involved. On the other hand, the broader extent of elevated Vp/Vs ratios >1.85 in the southern segment (P6-P10) are mainly related to the presence of the CR and its sharp topography (Figure S11). This bathymetric feature and the previously mentioned outer rise bending contribute to a deeply fractured and highly hydrated oceanic crust.

Low velocities in the oceanic crust

Our 3DVM illuminates a highly heterogeneous margin which is largely affected by the presence of topographic features on the seafloor. Horizontal slices at z=10 km (see Figure 6) show a prominent elongated N-S feature with Vp~5.5 km/s located ~10 km eastward of the trench axis. Restoring and resolution tests in Supplementary 5, 6, 7 and 8 support the robustness of this intriguing feature. Moreover, the inspection of the MRM along strike (Figure S12) show small SF and rounded 70% contour lines indicating a reduced along strike “smearing” and therefore a well resolved area. The along strike length of this anomaly (~130 km) is consistent with the incoming bathymetric structures in the area (see Figure S11). Moreover, lower Vp (~5.0 km/s) anomalies are confined to smaller areas in P4, P6-P7 and P9. These observations can be complemented by collocating the observed Vp to the imaged Vp/Vs ratios. Horizontal slices in Figure 6 allow us to estimate the dimension of the observed features by imaging a rounded, ~15 x 25 km2 (at z=10 km), low Vp/Vs ratios anomalies (~1.75), located around P4.

Cross sections in Figure 7 help us to discuss the in-depth extension of the observed anomalies. Here we focus on P4 which shows a prominent low Vp body (~5.0 – 5.5 km/s) at ~20 km from the trench that it is flanked by two areas with Vp~6.0 km/s on the sides. This feature agrees in shape and location with the observations described by Marcaillou et al. (2016) who estimated a ~2.5 km high seamount through an active seismic experiment. It also matches with the residual bathymetry derived by Agurto-Detzel et al. (2019 – see Figure S11). Therefore, we interpret the observed low Vp anomaly as a seamount coming from the Atacames seamount chain, in the northern edge of the CR, (P4, Vp~ 5.0 km/s) surrounded by Vp~5.5 km/s that could be related to possible thermal anomalies associated to the origin of these structures and/or possible serpentinization as observed farther north by Marcaillou et al. (2008).

The seismicity distribution also contributes to reinforce our interpretation. In P4 (see Figure 7), we observe two vertical clusters of aftershocks suggesting that the flanks of the seamount are under a high stress regime promoting faulting and seismic stress release. The clustered seismicity allows us to estimate a ~15-20 km lateral extension of this feature.

In relation to the origin of the observed low velocities studies in young seamounts have shown, that it is possible to observe low Vp in its structure (eg. Caplan-Auerbach et al., 2001; Kopp et al., 2009). In the case of the Ecuadorian margin, it has been estimated that the Atacames seamounts were created around ~20 - 15 Myr ago in the Galapagos hot-spot (Lonsdale, 1978; Sallares et al., 2003) which fits the young age hypothesis. Moreover, the erosive margin might have contributed to increasing the pressure along the seamount axis creating weaker areas in its base leading to the observed reduced velocities.

Further south, the relation between low Vp (~5.5 kms) and high Vp/Vs (>1.85) suggest a different interpretation for this segment. Between P6-P8, we observe a broader low Vp (~5.5 km/s) anomaly that might correspond to material of the CR. Moreover, the elevated Vp/Vs ratios (~1.85) imaged along P6-P10 might point to a deeply fractured and highly hydrated incoming CR.

Structures controlling the seismicity

Figures 6 and 7 show the distribution of the seismicity over both Vp and Vp/Vs 3DVM. Although most of the relocated aftershocks are distributed along the plate interface, we identified several clusters of seismicity that can be related to structural features imaged by our 3D velocity model.

As we mentioned before, in the subducting Nazca plate, between latitudes ~1°N and ~2°S, the Atacames seamounts and the CR contribute to increase deformation and therefore to creating and/or reactivating extensional faults in the Nazca plate. This process, plus the bending of the plate prior subducting that causes extensional faulting, facilitates the occurrence of clustered seismicity along small-scale faults in the oceanic crust (see Figure 8). In the case of the Atacames seamounts, its influence on the Ecuadorian margin can be observed in the bathymetry of the marine forearc (Von Huene et al., 2004; Collot et al., 2005; Barnes et al., 2010; Marcaillou et al., 2016), and also inferred by the seismicity detected at shallow depths in the marine eroded wedge suggesting a highly fractured region. Subducted seamounts can also act as asperities/barrier at greater depths (>15 km) contributing to the nucleation and/or stop of intermediate-magnitude (M 7.5 – 8.0, Bilek et al., 2003) megathrust earthquakes (Watts et al., 2010; Wang and Bilek, 2011).

The CR seems to be the main feature controlling the seismicity in the margin between P3-P10. Several studies have suggested that ridges may act aseismically and/or promote creep on the megathrust fault accompanied with small events (eg. Wang and Bilek, 2014). For the CR, Gutscher et al. (1999) described how large earthquakes have not ruptured across this feature. Graindorge et al. (2004) suggested a greater period of recurrence of large earthquakes in that region in comparison with the northern segment. Recently, Agurto-Detzel et al. (2019) also proposed differences on the slip behavior for North and South segments. Based on the imaged Vp and Vp/Vs models, we suggest that this large-scale marine feature might contribute to a deeply fractured and highly hydrated oceanic crust promoting the circulation of fluids to greater depths (~20-30 km). Fluids would change the local behavior on the slab interface from unstable slip to conditionally stable (Kodaira et al., 2004) and therefore impede the occurrence of large megathrust earthquakes. These conditionally stable parts seem also to be favorable for SSE (e.g. Tokai segment in Nankai trench) and has been described in the area by Rolandone et al., (2018).

In the upper crust, several small- to large-scale faults might have been activated after the 2016 Pedernales earthquake. The shallow clustered seismicity observed close to the Esmeraldas city (~1°N) is related to extensional mechanism (Agurto-Detzel et al., 2019; Hoskins et al., 2018) and can be associated to the activation of the Tanigüe fault (Michaud et al., 2014 - see F11 in Figure 1b) which may extend down to ~15 km reaching a low Vp/Vs rounded-like body (~1.80) capable to produce this type of confined aftershocks. To the south (~1°S), we observe clustered vertically-aligned seismicity, at ~10-15 km depth, in the southernmost profile P9. Figure 1b help us to relate these events with the surface projection of the El Aromo fault (F6) which has been previously described as an active structure by Segovia et al. (2018) and it is well imaged in our Vp/Vs model by a strong contrast between elevated and reduced ratios (Figure 7).

7. Conclusion

Using the unprecedented rapid deployment that recorded the aftershock sequence unfolded by the 2016 Pedernales earthquake, we built a high-quality dataset of manually picked P- and S-phases, which were used to derive a 3DVM for Vp velocities and Vp/Vs ratios. We imaged the seismotectonic and geological velocity structure of the central Ecuadorian subduction zone. Velocities (~4.5 km/s – 7.5 km/s) in the downgoing plate highlight the roughness of the incoming oceanic crust. Moreover, the observed Vp/Vs anomalies ranging from 1.74 to 1.95 suggest a heterogeneous and hydrated margin. We imaged the subduction of long-scale bathymetric features, such as the Atacames seamounts and the CR, which seems to contribute to the high circulation of fluids, especially close to the trench.

These features also play an important role in controlling the seismic behavior of the margin. We identified a subducting seamount, from the Atacames chain, with reduced Vp velocities (~5.0 km/s) and Vp/Vs ratios (1.75) associated with features with young magmatic material. On the other hand, the CR seems to be the main feature controlling the seismicity in the region, by promoting creeping and SSE caused by fluids migrating from a deeply fractured and highly hydrated oceanic crust. This fact is directly linked to the updip rupture limit of large megathrust earthquakes in the northern segment and the absence of large megathrust earthquakes in the southern region over the instrumental period.

Finally, our observations show the relevance of having well resolved Vp and Vp/Vs models that complement each other in order to give a full interpretation, especially in highly heterogeneous and segmented regions such as the Ecuadorian margin.

ACKNOWLEDGMENTS

This study was supported by IGEPN, IRD, the INSU-CNRS and the ANR grant REMAKE ANR-15-CE04-0004. The UK portion of the temporary deployment was supported by NERC grant NE/P008828/1. The US portion of the temporary deployment was supported by IRIS PASSCAL and NSF RAPID Program Award EAR-1642498. SLR acknowledges partial support from ANID under Programa Formación de Capital Humano Avanzado, Becas Chile (Grant 8068/2015). HAD acknowledges support from ANR project ANR-15-CE04-0004 and UCA/JEDI project ANR-15-IDEX-01. We are also indebted to the people at Geoazur laboratories and INOCAR by its contribution in the installation of OBSs at sea in very harsh environments. Also we extend the acknowledgment to the staff at IGEPN for the continuous support during the deployment and service of the inland stations.

Data available at IRIS website http://www.iris.edu/dms/nodes/dmc/ using the network code 8G (Meltzer and Beck, 2016), EC (Alvarado et al., 2018) and G (IGEP and EOST, 1982). Data from the emergency deployment XE available through Regnier et al., 2016. Aftershocks catalogue is available through Agurto-Detzel et al., 2019. Model data will be available in the KIT open repository. Finally, the authors want to thank all the people in Ecuador who allowed us to install our stations in their houses, big thanks for your hospitality, patience and help when it was needed.

References

Abe, K. (1979). Size of great earthquakes of 1837–1974 inferred from tsunami data. *Journal of Geophysical Research: Solid Earth*, *84*(B4), 1561-1568.

Agudelo, W., Ribodetti, A., Collot, J. Y., & Operto, S. (2009). Joint inversion of multichannel seismic reflection and wide-angle seismic data: Improved imaging and refined velocity model of the crustal structure of the North Ecuador–South Colombia convergent margin. *Journal of Geophysical Research: Solid Earth*, *114*(B2).

Agurto-Detzel, H., Font, Y., Charvis, P., Rietbrock, A., Ambrois, D., Paullato, M., ... Soto-Cordero, L. (2019). Ridge subduction and afterslip control aftershock distribution of the 2016 Mw 7.8 Ecuador earthquake. *Earth and Planetary Science Letters*.

Agurto, H., Rietbrock, A., Barrientos, S., Bataille, K., & Legrand, D. (2012). Seismo-tectonic structure of the Aysén Region, Southern Chile, inferred from the 2007 M w= 6.2 Aysén earthquake sequence. *Geophysical Journal International*, *190*(1), 116-130.

Alvarado, A., Audin, L., Nocquet, J. M., Jaillard, E., Mothes, P., Jarrín, P., ... & Cisneros, D. (2016). Partitioning of oblique convergence in the Northern Andes subduction zone: Migration history and the present-day boundary of the North Andean Sliver in Ecuador. *Tectonics*, *35*(5), 1048-1065.

Alvarado, A., Ruiz, M., Mothes, P., Yepes, H., Segovia, M., Vaca, M., ... & Aguilar, J. (2018). Seismic, volcanic, and geodetic networks in Ecuador: Building capacity for monitoring and research. *Seismological Research Letters*, *89*(2A), 432-439.

Araujo, S. (2013). The Ecuadorian moho. *La Granja*,*18*(2), 43-47.

Araujo, S. (2016). *Travel time tomography of the crust and the mantle beneath Ecuador from data of the national seismic network* (Doctoral dissertation, Grenoble Alpes).

Bangs, N. L., McIntosh, K. D., Silver, E. A., Kluesner, J. W., & Ranero, C. R. (2015). Fluid accumulation along the Costa Rica subduction thrust and development of the seismogenic zone. *Journal of Geophysical Research: Solid Earth*, *120*(1), 67-86.

Barnes, P. M., Lamarche, G., Bialas, J., Henrys, S., Pecher, I., Netzeband, G. L., ... & Crutchley, G. (2010). Tectonic and geological framework for gas hydrates and cold seeps on the Hikurangi subduction margin, New Zealand. *Marine Geology*, *272*(1-4), 26-48.

Beck, S. L., and L. J. Ruff (1984). The rupture process of the great 1979 Colombia earthquake: Evidence for the asperity model, *J. Geophys. Res*., 89, 9281-9291.

Bilek, S. L., Schwartz, S. Y., & DeShon, H. R. (2003). Control of seafloor roughness on earthquake rupture behavior. *Geology*, *31*(5), 455-458.

Bilek, S. L. (2010). Invited review paper: Seismicity along the South American subduction zone: Review of large earthquakes, tsunamis, and subduction zone complexity. *Tectonophysics*, *495*(1-2), 2-14.

Calahorrano, A., Sallarès, V., Collot, J. Y., Sage, F., & Ranero, C. R. (2008). Nonlinear variations of the physical properties along the southern Ecuador subduction channel: Results from depth-migrated seismic data. *Earth and Planetary Science Letters*, *267*(3-4), 453-467.

Cantalamessa, G., Di Celma, C., Ragaini, L., Valleri, G., & Landini, W. (2007). Sedimentology and high-resolution sequence stratigraphy of the late middle to late Miocene Angostura Formation (western Borbón Basin, northwestern Ecuador). *Journal of the Geological Society*, *164*(3), 653-665.

Caplan-Auerbach, J., & Duennebier, F. K. (2001). Seismicity and velocity structure of Loihi Seamount from the 1996 earthquake swarm. *Bulletin of the Seismological Society of America*, *91*(2), 178-190.

Cerpa, N. G., R. Araya, M. Gerbault, and R. Hassani (2015), Relationship between slab dip and topography segmentation in an oblique subduction zone: Insights from numerical modeling, *Geophysical Research Letters*, 42.

Chambat, F., & Valette, B. (1996). Figure non hydrostatique des planètes: inversion gravimétrique et modèles 3D de la Terre et de la Lune. *srst*, 69-74.

Chlieh, M., Mothes, P. A., Nocquet, J. M., Jarrin, P., Charvis, P., Cisneros, D., ... & Vallée, M. (2014). Distribution of discrete seismic asperities and aseismic slip along the Ecuadorian megathrust. *Earth and Planetary Science Letters*, *400*, 292-301.

Collings, R., Lange, D., Rietbrock, A., Tilmann, F., Natawidjaja, D., Suwargadi, B., ... & Saul, J. (2012). Structure and seismogenic properties of the Mentawai segment of the Sumatra subduction zone revealed by local earthquake traveltime tomography. *Journal of Geophysical Research: Solid Earth*, *117*(B1).

Collot, J. Y., Charvis, P., Gutscher, M. A., & Operto, S. (2002). Exploring the Ecuador‐Colombia active margin and interplate seismogenic zone. *EOS, Transactions American Geophysical Union*, *83*(17), 185-190.

Collot, J. Y., Marcaillou, B., Sage, F., Michaud, F., Agudelo, W., Charvis, P., ... & Spence, G. (2004). Are rupture zone limits of great subduction earthquakes controlled by upper plate structures? Evidence from multichannel seismic reflection data acquired across the northern Ecuador–southwest Colombia margin. *Journal of Geophysical Research: Solid Earth*, *109*(B11).

Collot, J. Y., Michaud, F., Alvarado, A., Marcaillou, B., Sosson, M., Ratzov, G., ... & Pazmino, A. (2009). Visión general de la morfología submarina del margen convergente de Ecuador-Sur de Colombia: implicaciones sobre la transferencia de masa y la edad de la subducción de la Cordillera de Carnegie. *En Geología y Geofísica Marina y Terrestre del Ecuador*.

Collot, J. Y., Migeon, S., Spence, G., Legonidec, Y., Marcaillou, B., Schneider, J. L., ... & Pazmino, A. (2005). Seafloor margin map helps in understanding subduction earthquakes. *Eos*, *Transactions American Geophysical Union*, *86*(46), 463-465.

Collot, J. Y., Sanclemente, E., Nocquet, J. M., Leprêtre, A., Ribodetti, A., Jarrin, P., ... & Charvis, P. (2017). Subducted oceanic relief locks the shallow megathrust in central Ecuador. *Journal of Geophysical Research: Solid Earth*, *122*(5), 3286-3305.

Contreras-Reyes, E., Jara, J., Grevemeyer, I., Ruiz, S., & Carrizo, D. (2012). Abrupt change in the dip of the subducting plate beneath north Chile. *Nature Geoscience*, *5*(5), 342-345.

Christensen, N. I. (1996). Poisson's ratio and crustal seismology. *Journal of Geophysical Research: Solid Earth*, *101*(B2), 3139-3156.

Christensen, N. I. (2004). Serpentinites, peridotites, and seismology. *International Geology Review*, *46*(9), 795-816.

Dominguez, S., Lallemand, S. E., Malavieille, J., & von Huene, R. (1998). Upper plate deformation associated with seamount subduction. *Tectonophysics*, *293*(3-4), 207-224.

Dorbath, L., Cisternas, A., & Dorbath, C. (1990). Assessment of the size of large and great historical earthquakes in Peru. *Bulletin of the Seismological Society of America*, *80*(3), 551-576.

Eberhart-Phillips, D. (1990), Three-dimensional P and S velocity structure in the Coalinga region, California, J. Geophys. Res., 95, 15,343–15,363.

Egred, J. (1968). Breve historia sísmica de la República del Ecuador (1534-1965). *Bol. Bibl. Geofís. Oceanogr. Am*.

Evans, J. R., D. Eberhart-Phillips, and C. H. Thurber (1994), User's manual for SIMULPS12 for imaging Vp and Vp/Vs: A derivative of the “Thurber” tomographic inversion SIMUL3 for local earthquakes and explosions, U.S. Geol. Surv. Open File Rep., 94-431.

Feininger, T., & Seguin, M. K. (1983). Simple Bouguer gravity anomaly field and the inferred crustal structure of continental Ecuador. *Geology*, *11*(1), 40-44.

Font, Y., Segovia, M., Vaca, S., & Theunissen, T. (2013). Seismicity patterns along the Ecuadorian subduction zone: new constraints from earthquake location in a 3-D a priori velocity model. *Geophysical Journal International*, *193*(1), 263-286.

Gailler, A., Charvis, P., & Flueh, E. R. (2007). Segmentation of the Nazca and South American plates along the Ecuador subduction zone from wide angle seismic profiles. *Earth and Planetary Science Letters*, *260*(3-4), 444-464.

Garcia‐Cano, L. C. G., Galve, A., Charvis, P., & Marcaillou, B. (2014). Three‐dimensional velocity structure of the outer fore arc of the Colombia‐Ecuador subduction zone and implications for the 1958 megathrust earthquake rupture zone. *Journal of Geophysical Research: Solid Earth*, *119*(2), 1041-1060.

Graindorge, D., Calahorrano, A., Charvis, P., Collot, J. Y., & Bethoux, N. (2004). Deep structures of the Ecuador convergent margin and the Carnegie Ridge, possible consequence on great earthquakes recurrence interval. *Geophysical Research Letters*, *31*(4).

Gutscher, M. A., Malavieille, J., Lallemand, S., & Collot, J. Y. (1999). Tectonic segmentation of the North Andean margin: impact of the Carnegie Ridge collision. *Earth and Planetary Science Letters*, *168*(3-4), 255-270.

Hacker, B. R., Abers, G. A., & Peacock, S. M. (2003). Subduction factory 1. Theoretical mineralogy, densities, seismic wave speeds, and H2O contents. *Journal of Geophysical Research: Solid Earth*, *108*(B1).

Hacker, B. R., Peacock, S. M., Abers, G. A., & Holloway, S. D. (2003). Subduction factory 2. Are intermediate-depth earthquakes in subducting slabs linked to metamorphic dehydration reactions?. *Journal of Geophysical Research: Solid Earth*, *108*(B1).

Hardy, N. C. (1991). Tectonic evolution of the easternmost Panama Basin: Some new data and inferences. *Journal of South American earth sciences*, *4*(3), 261-269.

Hayes, G. P., Wald, D. J., & Johnson, R. L. (2012). Slab1. 0: A three-dimensional model of global subduction zone geometries. *Journal of Geophysical Research: Solid Earth*, *117*(B1).

Herd, D. G., Youd, T. L., Meyer, H., Person, W. J., & Mendoza, C. (1981). The great tumaco, colombia earthquake of 12 december 1979. *Science*, *211*(4481), 441-445.

Hicks, S. P., Rietbrock, A., Ryder, I. M., Lee, C. S., & Miller, M. (2014). Anatomy of a megathrust: The 2010 M8. 8 Maule, Chile earthquake rupture zone imaged using seismic tomography. *Earth and Planetary Science Letters*, *405*, 142-155.

Hoskins, M., Meltzer, A., Soto-Cordero, L., Stachnik, J., Lynner, C., Ruiz, M., ... & Nocquet, J. M. (2018, May). Postseismic deformation: the Esmeraldas, Ecuador Seismic sequence Following the 2016 Pedernales Megathrust Earthquake. In *SSA Seismology of the Americas Meeting*.

Husen, S., Kissling, E., & Flueh, E. R. (2000). Local earthquake tomography of shallow subduction in north Chile: A combined onshore and offshore study. *Journal of Geophysical Research: Solid Earth*, *105(B12)*, 28183-28198.

Hyndman, R. D. (1979). Poisson's ratio in the oceanic crust—a review. *Tectonophysics*, *59*(1-4), 321-333.

IPGP (Institut De Physique Du Globe De Paris) and EOST (Ecole Et Observatoire Des Sciences De La Terre De Strasbourg), 1982. GEO-SCOPE, French Global Network of broad band seismic stations. Institut de Physique du Globe de Paris (IPGP). Other/Seismic Network.

Ito, A., Fujie, G., Miura, S., Kodaira, S., Kaneda, Y., & Hino, R. (2005). Bending of the subducting oceanic plate and its implication for rupture propagation of large interplate earthquakes off Miyagi, Japan, in the Japan Trench subduction zone. *Geophysical Research Letters*, *32*(5).

Jaillard, E., Hérail, G., Monfret, T., Díaz-Martínez, E., Baby, P., Lavenu, A., & Dumont, J. F. (2000). Tectonic evolution of the Andes of Ecuador, Peru, Bolivia and northernmost Chile. *Tectonic Evolution of South America*, *31*, 481-559.

Jaillard, E., Lapierre, H., Ordóñez, M., Toro, J., Amórtegui, A., & Vanmelle, J. (2009). Accreted oceanic terranes in Ecuador: southern edge of the Caribbean Plate? Geological Society, London, Special Publications, 328, 469–485.Kanamori, H., & McNally, K. C. (1982). Variable rupture mode of the subduction zone along the Ecuador-Colombia coast. *Bulletin of the Seismological Society of America*, *72*(4), 1241-1253.

Kato, A., Iidaka, T., Ikuta, R., Yoshida, Y., Katsumata, K., Iwasaki, T., ... & Watanabe, T. (2010). Variations of fluid pressure within the subducting oceanic crust and slow earthquakes. *Geophysical research letters*, *37*(14).

Kelleher, J. A. (1972). Rupture zones of large South American earthquakes and some predictions. *Journal of Geophysical Research*, *77*(11), 2087-2103.

Kendrick, E., Bevis, M., Smalley Jr, R., Brooks, B., Vargas, R. B., Laurıa, E., & Fortes, L. P. S. (2003). The Nazca–South America Euler vector and its rate of change. *Journal of South American Earth Sciences*, *16*(2), 125-131.

Koch, C. D., Lynner, C., Delph, J., Beck, S. L., Meltzer, A., Font, Y., ... & Alvarado, A. (2020). Structure of the Ecuadorian forearc from the joint inversion of receiver functions and ambient noise surface waves. *Geophysical Journal International*, 222 (3).

Kodaira, S., Iidaka, T., Kato, A., Park, J. O., Iwasaki, T., & Kaneda, Y. (2004). High pore fluid pressure may cause silent slip in the Nankai Trough. *Science*, *304*(5675), 1295-1298.

Kopp, H., Flueh, E. R., Papenberg, C., & Klaeschen, D. (2004). Seismic investigations of the O'Higgins Seamount Group and Juan Fernández Ridge: aseismic ridge emplacement and lithosphere hydration. *Tectonics*, *23*(2).

Lee, W. H. K., & Lahr, J. C. (1972). *HYPO71: A computer program for determining hypocenter, magnitude, and first motion pattern of local earthquakes* (No. 72-224). US Geological Survey,.

León-Ríos, S., Agurto-Detzel, H., Rietbrock, A., Alvarado, A., Beck, S., Charvis, P., ... & Lynner, C. (2019). 1D-velocity structure and seismotectonics of the Ecuadorian margin inferred from the 2016 Mw7. 8 Pedernales aftershock sequence. *Tectonophysics*, *767*, 228165.

Lonsdale, P. (1978). Ecuadorian subduction system. *AAPG Bulletin*, *62*(12), 2454-2477.

Lonsdale, P. (2005). Creation of the Cocos and Nazca plates by fission of the Farallon plate. *Tectonophysics*, *404*(3), 237-264.

Luzieux, L. D. A., Heller, F., Spikings, R., Vallejo, C. F., & Winkler, W. (2006). Origin and Cretaceous tectonic history of the coastal Ecuadorian forearc between 1 N and 3 S: Paleomagnetic, radiometric and fossil evidence. *Earth and Planetary Science Letters*, *249*(3-4), 400-414.

Lynner, C., Koch, C., Beck, S. L., Meltzer, A., Soto-Cordero, L., Hoskins, M. C., ... & Font, Y. (2020). Upper-plate structure in Ecuador coincident with the subduction of the Carnegie Ridge and the southern extent of large mega-thrust earthquakes. *Geophysical Journal International*, *220*(3), 1965-1977.

Marcaillou, B., Spence, G., Wang, K., Collot, J. Y., & Ribodetti, A. (2008). Thermal segmentation along the N. Ecuador–S. Colombia margin (1–4 N): Prominent influence of sedimentation rate in the trench. *Earth and Planetary Science Letters*, *272*(1-2), 296-308.

Marcaillou, B., Collot, J. Y., Ribodetti, A., d'Acremont, E., Mahamat, A. A., & Alvarado, A. (2016). Seamount subduction at the North-Ecuadorian convergent margin: Effects on structures, inter-seismic coupling and seismogenesis. *Earth and Planetary Science Letters*, *433*, 146-158.

Meissnar, R. O., Flueh, E. R., Stibane, F., & Berg, E. (1976). Dynamics of the active plate boundary in southwest Colombia according to recent geophysical measurements. *Tectonophysics*, *35*(1-3), 115-136.

Meltzer, A. & Beck, S.L., 2016. Pedernales Earthquake Aftershock Deployment Ecuador. International Federation of Digital Seismograph Networks. Other/Seismic Network.

Meltzer, A., Beck, S., Ruiz, M., Hoskins, M., Soto-Cordero, L., Stachnik, J. C., ... Mercerat, E. D. (2019). The 2016 Mw 7.8 Pedernales Earthquake, Ecuador: RAPID Response Deployment. *Seismological Research Letters*.

Menant, A., Angiboust, S., & Gerya, T. (2019). Stress-driven fluid flow controls long-term megathrust strength and deep accretionary dynamics. *Scientific reports*, *9*(1), 1-11.

Mendoza, C., & Dewey, J. W. (1984). Seismicity associated with the great Colombia-Ecuador earthquakes of 1942, 1958, and 1979: Implications for barrier models of earthquake rupture. *Bulletin of the seismological society of America*, *74*(2), 577-593.

Michaud, F., Proust, J. N., Collot, J. Y., Lebrun, J. F., Witt, C., Ratzov, G., ... & Penafiel, L. (2015). Quaternary sedimentation and active faulting along the Ecuadorian shelf: preliminary results of the ATACAMES Cruise (2012). *Marine Geophysical Research*, *36*(1), 81-98.

Mothes, P. A., Nocquet, J. M., & Jarrín, P. (2013). Continuous GPS network operating throughout Ecuador. *Eos, Transactions American Geophysical Union*, *94*(26), 229-231.

Nocquet, J. M., Mothes, P., & Alvarado, A. (2009). Geodesia, geodinámica y ciclo sísmico en Ecuador. *Geologia y Geofisica Marina y Terrestre del Ecuador. Edited by JY Collot et al*, 83-95.

Nocquet, J. M., Jarrin, P., Vallée, M., Mothes, P. A., Grandin, R., Rolandone, F., ... & Régnier, M. (2017). Supercycle at the Ecuadorian subduction zone revealed after the 2016 Pedernales earthquake. *Nature Geoscience*, *10*(2), 145-149.

Pasten-Araya, F., Salazar, P., Ruiz, S., Rivera, E., Potin, B., Maksymowicz, A., et al (2018). Fluids along the plate interface influencing the frictional regime of the Chilean Subduction zone, northern Chile. *Geophysical Research Letters*, 45.

Peacock, S. M. (2001). Are the lower planes of double seismic zones caused by serpentine dehydration in subducting oceanic mantle?. *Geology*, *29*(4), 299-302.

Regnier, M., Font, Y., Charvis, P., Mercerat, D., Rietbrock, A., Ruiz, M. & Alvarado, A., 2016. Pedernales. International Federation of Digital Seismograph Networks. Dataset/Seismic Network.

Reguzzoni, M., & Sampietro, D. (2012). Moho estimation using GOCE data: a numerical simulation. In *Geodesy for Planet Earth* (pp. 205-214). Springer, Berlin, Heidelberg.

Reyes, P., & Michaud, F. (2012). Mapa Geológico de la Margen Costera Ecuatoriana (1500000) EPPetroEcuador-IRD. *Quito Ecuador*.

Rolandone, F., Nocquet, J. M., Mothes, P. A., Jarrin, P., Vallée, M., Cubas, N., ... & Font, Y. (2018). Areas prone to slow slip events impede earthquake rupture propagation and promote afterslip. *Science advances*, *4*(1), eaao6596.

Sallarès, V., & Charvis, P. (2003). Crustal thickness constraints on the geodynamic evolution of the Galapagos Volcanic Province. *Earth and Planetary Science Letters*, *214*(3-4), 545-559.

Sallarès, V., & Ranero, C. R. (2005). Structure and tectonics of the erosional convergent margin off Antofagasta, north Chile (23 30' S). *Journal of Geophysical Research: Solid Earth*, *110*(B6).

Sallarès, V., Charvis, P., Flueh, E. R., Bialas, J., & SALIERI Scientific Party. (2005). Seismic structure of the Carnegie ridge and the nature of the Galapagos hotspot. *Geophysical Journal International*, *161*(3), 763-788.

Segovia, M. (2001). El sismo de Bahía del 4 de agosto de 1998: Caracterización del mecanismo de ruptura y análisis de la sismicidad en la zona costera. *Título de Ingeniera Geología (tesis): Escuela Politécnica Nacional*, *Quito*, *Ecuador*.

Segovia, M., Alvarado, A., Collot, J. Y., Sallares, V., & Pazmiño, N. (2009). Breve análisis de la sismicidad y del campo de esfuerzos en el Ecuador. *Geología y Geofísica Marina y Terrestre del Ecuador: desde la costa continental hasta las Islas Galápagos*, 131-149.

Segovia, M., Font, Y., Régnier, M., Charvis, P., Galve, A., Nocquet, J. M., ... & Pazmiño, A. (2018). Seismicity Distribution Near a Subducting Seamount in the Central Ecuadorian Subduction Zone, Space-Time Relation to a Slow-Slip Event. *Tectonics*,*37*(7), 2106-2123.

Sennson, J. L., & Beck, S. L. (1996). Historical 1942 Ecuador and 1942 Peru subduction earthquakes and earthquake cycles along Colombia-Ecuador and Peru subduction segments. *Pure and applied geophysics*, *146*(1), 67-101.

Soto-Cordero, L., Meltzer, A., Bergman, E., Hoskins, M., Stachnik, J. C., Agurto-Detzel, H., ... & Hayes, G. P. (2020). Structural Control on Megathrust Rupture and Slip Behavior: Insights From the 2016 Mw 7.8 Pedernales Ecuador Earthquake. *Journal of Geophysical Research: Solid Earth*, *125*(2), e2019JB018001.

Spakman, W., & Nolet, G. (1988). Imaging algorithms, accuracy and resolution in delay time tomography. In *Mathematical geophysics*(pp. 155-187). Springer, Dordrecht.

Staudigel, H., Park, K. H., Pringle, M., Rubenstone, J. L., Smith, W. H. F., & Zindler, A. (1991). The longevity of the South Pacific isotopic and thermal anomaly. *Earth and Planetary Science Letters*, *102*(1), 24-44.

Storchak, D. A., Di Giacomo, D., Bondár, I., Engdahl, E. R., Harris, J., Lee, W. H., ... & Bormann, P. (2013). Public release of the ISC–GEM global instrumental earthquake catalogue (1900–2009). *Seismological Research Letters*, *84*(5), 810-815.

Thurber, C. H. (1983), Earthquake locations and three-dimensional crustal structure in the Coyote Lake area, central California, J. Geophys. Res., 88, 8226–8236.

Thurber, C. H. (1993), Local earthquake tomography: velocities and Vp/Vs-theory, in Seismic Tomography: Theory and Practice, edited by H. M. Iyer, and K. Hirahara, pp. 563–583, Chapman and Hall, London.

Trenkamp, R., Kellogg, J. N., Freymueller, J. T., & Mora, H. P. (2002). Wide plate margin deformation, southern Central America and northwestern South America, CASA GPS observations. *Journal of South American Earth Sciences*, *15*(2), 157-171.

Vaca, S., Régnier, M., Bethoux, N., Alvarez, V., & Pontoise, B. (2009). Sismicidad de la región de Manta: Enjambre sísmico de Manta-2005. *Geologia y Geofisica Marina y Terrestre del Ecuador Desde la Costa Continental Hasta las Islas Galapagos*, 151-166.

Vaca, S., Vallée, M., Nocquet, J. M., Battaglia, J., & Régnier, M. (2018). Recurrent slow slip events as a barrier to the northward rupture propagation of the 2016 Pedernales earthquake (Central Ecuador). *Tectonophysics*, *724*, 80-92.

Vallée, M., Nocquet, J. M., Battaglia, J., Font, Y., Segovia, M., Regnier, M., ... & Yepes, H. (2013). Intense interface seismicity triggered by a shallow slow slip event in the Central Ecuador subduction zone. *Journal of Geophysical Research: Solid Earth*, *118*(6), 2965-2981.

von Huene, R., & Culotta, R. (1989). Tectonic erosion at the front of the Japan Trench convergent margin. *Tectonophysics*, *160*(1-4), 75-90.

von Huene, R., Ranero, C. R., Weinrebe, W., & Hinz, K. (2000). Quaternary convergent margin tectonics of Costa Rica, segmentation of the Cocos Plate, and Central American volcanism. *Tectonics*, *19*(2), 314-334.

von Huene, R., Ranero, C. ., & Watts, P. (2004). *Tsunamigenic slope failure along the Middle America Trench in two tectonic settings. Marine Geology, 203(3-4), 303–317.*

von Huene, R., Ranero, C. R., & Vannucchi, P. (2004). Generic model of subduction erosion. *Geology*, *32*(10), 913-916.

Wang, K., & Bilek, S. L. (2011). Do subducting seamounts generate or stop large earthquakes? *Geology*, *39*(9), 819-822.

Watts, A. B., Koppers, A. A., & Robinson, D. P. (2010). Seamount subduction and earthquakes. *Oceanography*, *23*(1), 166-173.

White, R. S., McKenzie, D., & O'Nions, R. K. (1992). Oceanic crustal thickness from seismic measurements and rare earth element inversions. *Journal of Geophysical Research: Solid Earth*, *97*(B13), 19683-19715.

Journal of Geophysical Research

Supporting information for

3D local earthquake tomography of the Ecuadorian margin in the source area of the 2016 Mw 7.8 Pedernales earthquake

Sergio León-Ríos[1*], Lidong Bie[1], Hans Agurto-Detzel[2], Andreas Rietbrock[1], Audrey Galve[2], Alexandra Alvarado[3], Susan Beck[4], Philippe Charvis[2], Yvonne Font[2], Silvana Hidalgo[3], Mariah Hoskins[5], Mireille Laigle[2], Davide Oregioni[2], Anne Meltzer[5], Mario Ruiz[3] and Jack Wollam[1]

1. Karlsruhe Institute of Technology, Geophysical Institute, Karlsruhe, 76187, Germany
2. Université Côte d'Azur, IRD, CNRS, Observatoire de la Côte d'Azur, Géoazur, 06304, Nice, France
3. Instituto Geofísico, Escuela Politécnica Nacional, Quito, 170525, Ecuador
4. Department of Geosciences, University of Arizona, Tucson, AZ 95721, USA
5. Department of Earth and Environmental Sciences, Lehigh University, Bethlehem, PA 18015, USA

Contents of this file

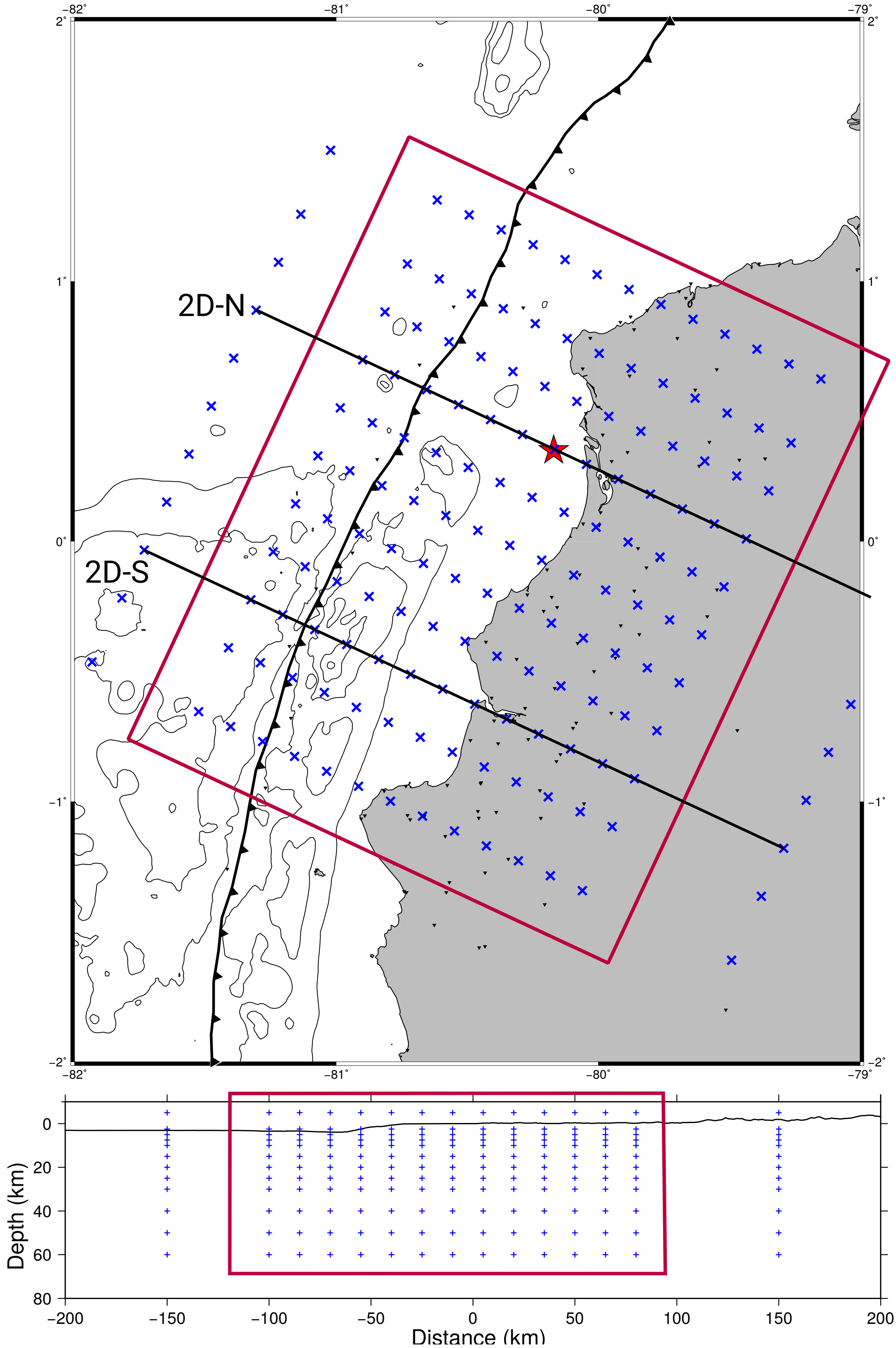

Figure S 1: Grid nodes distribution for the inversion process. Outer rectangle shows the distribution for the coarse grid, while inner rectangle represents the fine grid with a 15 km W-E nodes spacing and 22.5 km separation along strike. Bottom image shows the distribution in depth following the layering of the minimum 1D velocity model (Leon-Rios et al., 2019).

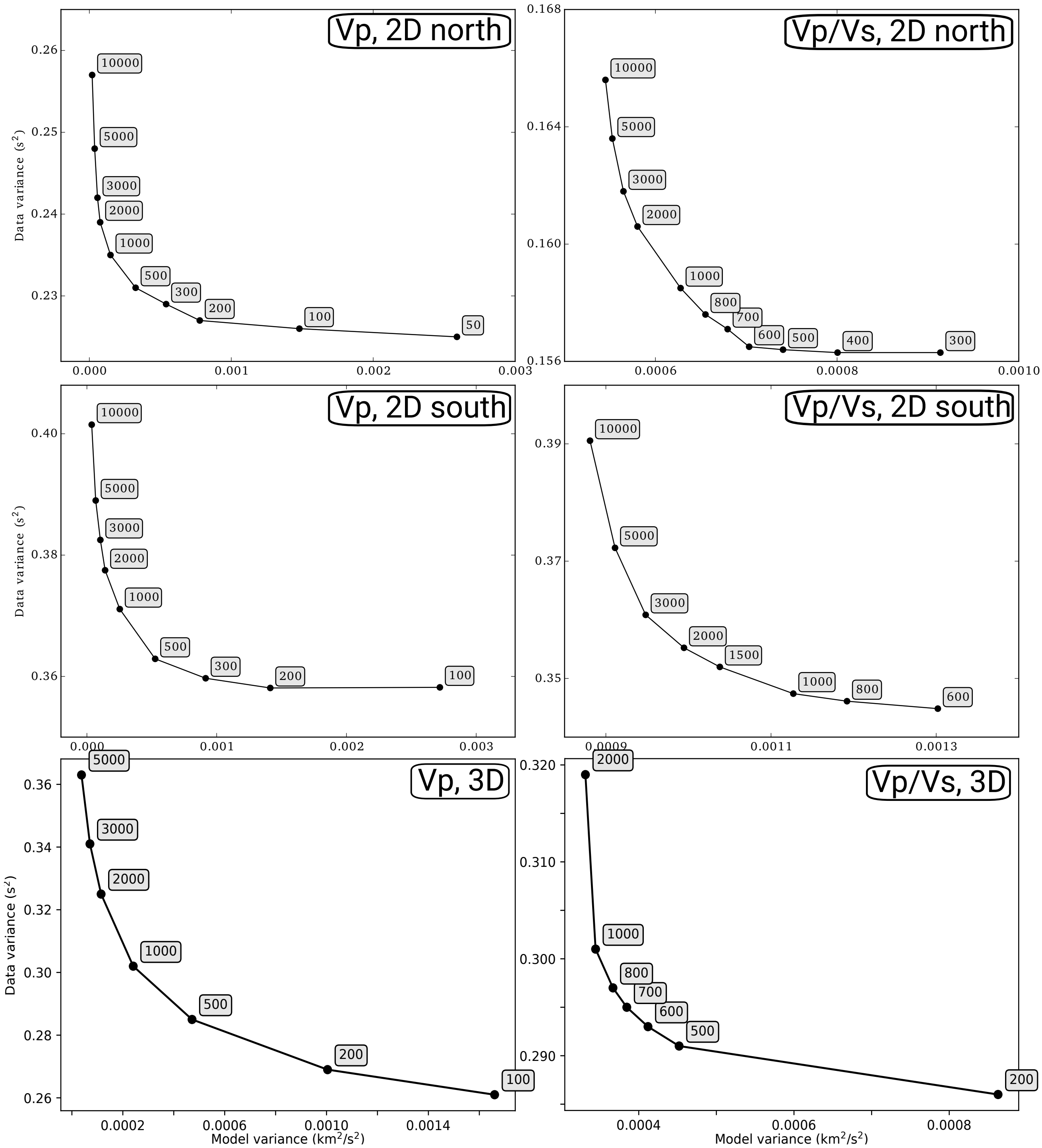

Figure S 2: Damping curves. Trade-off curves analysis for the different stages of this work. Left side shows the Vp and right side the Vp/Vs ratio. Damping curves were calculated for north and south segments in the 2D inversion, and for the complete dataset in the 3D inversion stage.

Figure S 3: MRM analysis. Model resolution matrix analysis using the spread function and the 70% of the diagonal elements of the MRM. Spread function is color coded with a blue-red with blue colors representing well resolved regions.

Figure S 4: Checkerboard test. Synthetic recovery test for left) small, 15km and rgiht) medium, 30 km anomalies. Top image show the input model comprised by alternated positive and negative anomalies of ± 5% of the inverted model. Bottom images show the recovered velocities along representative pro les for the northern, central and southern segments in our region of interest.

Figure S 6: Synthetic restoring test to evaluate the in uence of our 2D Vp northern segment model (2D-N), over a homogeneous subduction zone. Synthetic arrival times were generated using the synthetic model (2D-N) and then tested over the homogeneous initial model. Recovered velocities are shown for central pro les (P3-P8).

Figure S 8: 3D velocity model, merging modeling strategy. Cross sections. Three-dimensional models for both Vp (left) and Vp/Vs (right) based on a 2D-N and 2D-S merged initial model. Results are shown along 10 W-E pro les. Vp velocities and Vp/Vs ratios are color coded and iso-contours are plotted every 1.0 km/s and 0.025 for Vp and Vp/Vs, respectively. Based on the MRM and checkerboard test, non resolved areas are faded. Location of pro les, P1-P10, is shown in Figure 1. Width for projection of hypocenters and stations is 22 km. Relocated hypocenters are plotted in black circles, and stations are represented by inverted triangles. Grid nodes are displayed in black crosses and solid black triangles represent the projection of the trench and coastline. Yellow star in P3 indicates the hypocenter for the 2016 Pedernales earthquake (Nocquet et al., 2017). Modi ed slab interface (see main text for further details) is represented by solid black line.

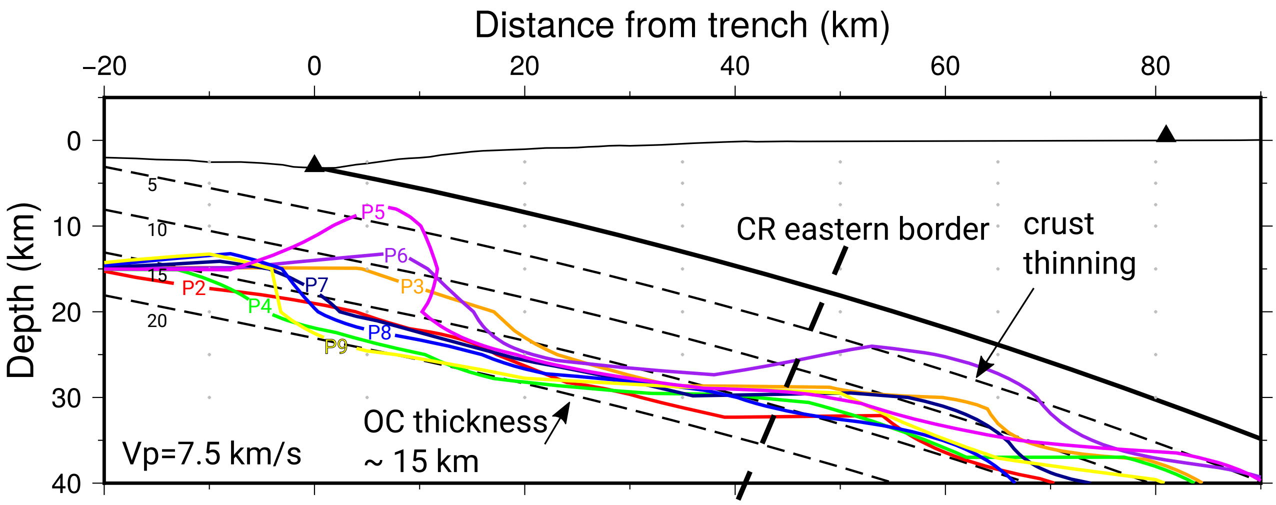

Figure S 10: Analyzing Vp iso-velocity contours. Vp velocities associated to the oceanic upper mantle (bottom). Cross sections compare the depth of profiles P2-P9 identified by colored solid lines. Slab interface and its projection at 5, 10 , 15 and 20 km are plotted for reference. Black triangle represents the trench.

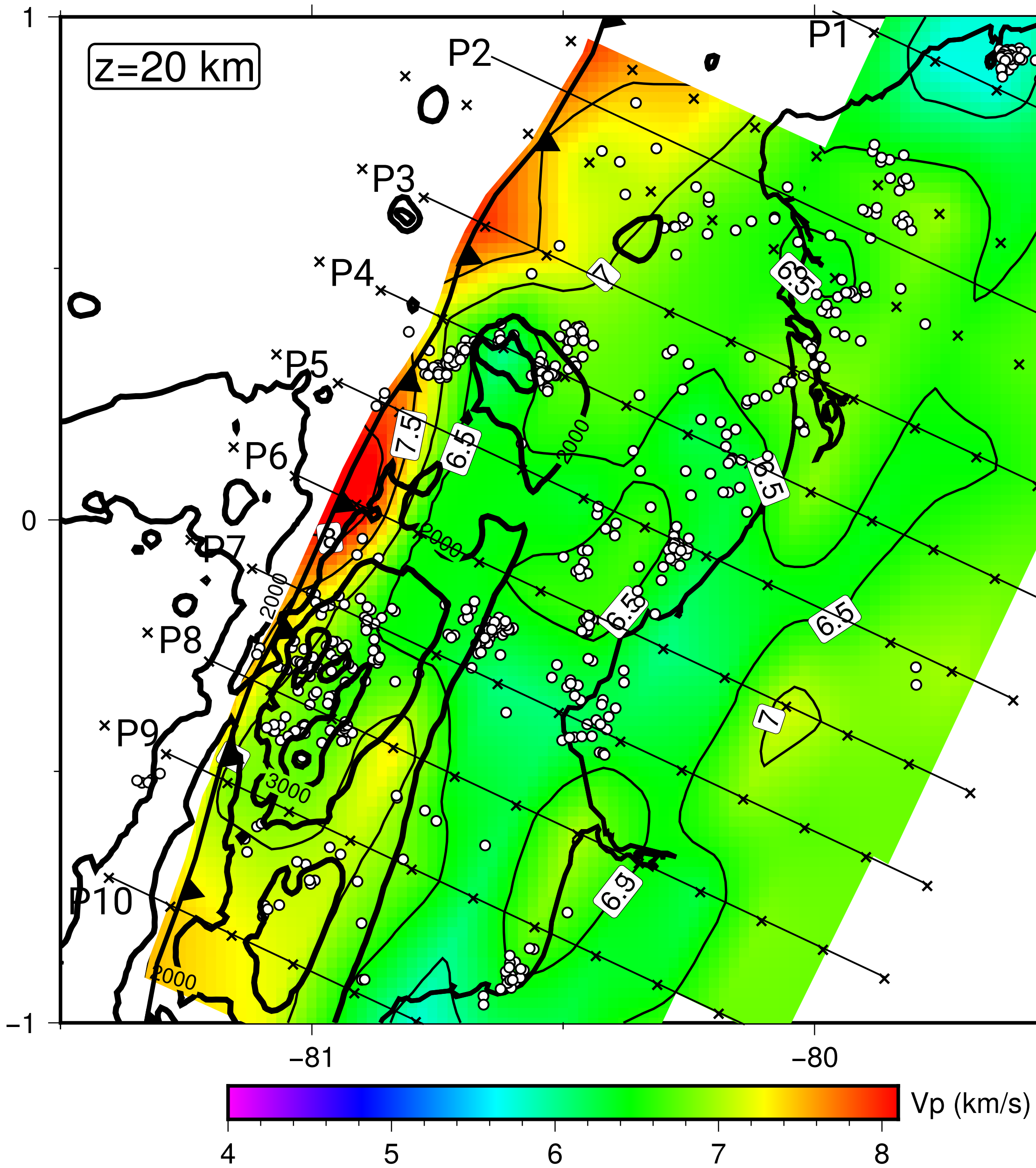

Figure S 11: Constrasting residual bathymetry and Vp horizontal slice. Residual bathymetry derived by Agurto-Detzel et al (2019) superimposed over our 3D Vp velocities obtained for a horizontal slice at 10 km depth.

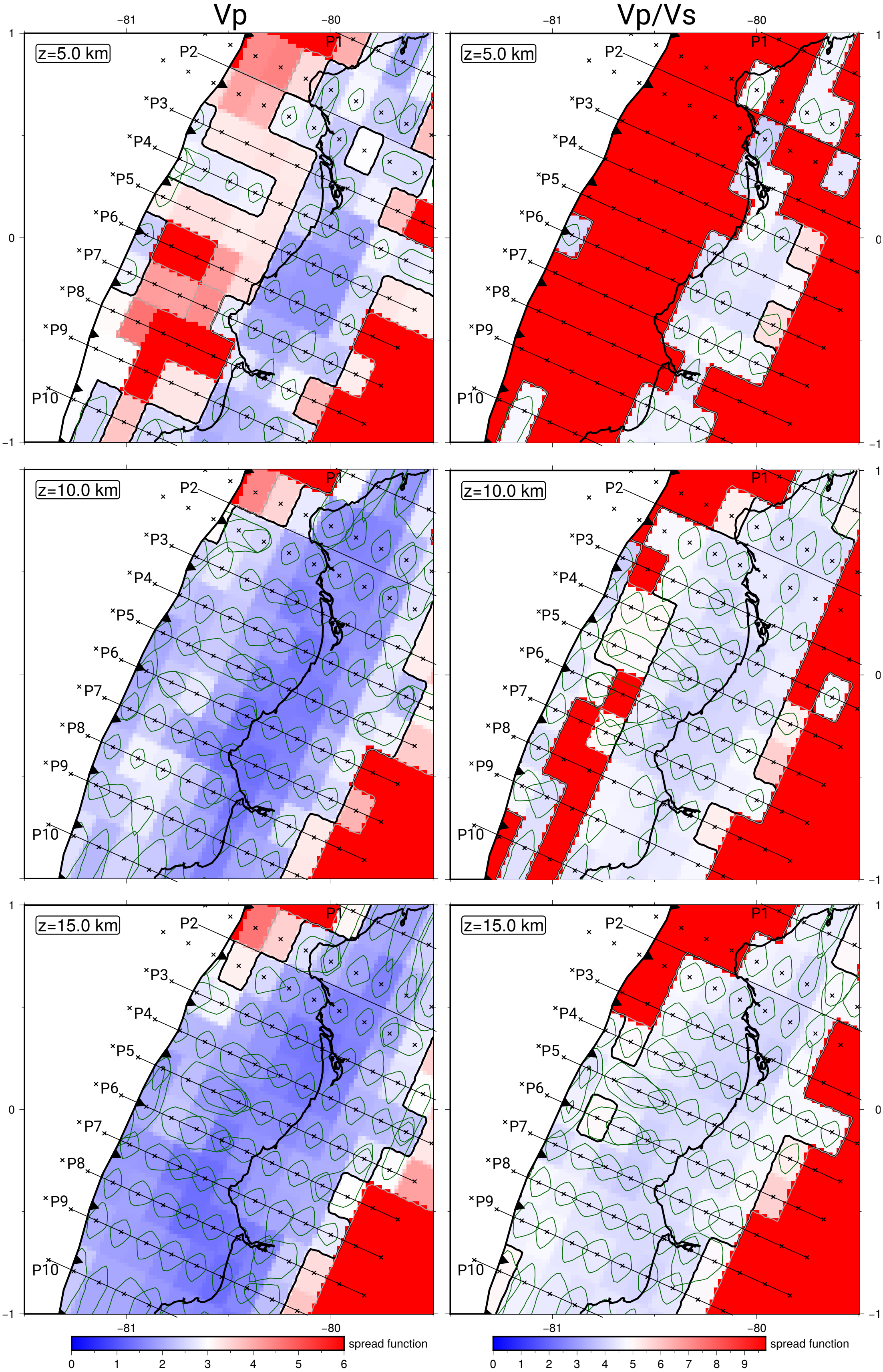

Figure S 12: MRM analysis along strike. Horizontal slices for the obtained 3D Vp (left) and Vp/Vs (right) models at 5, 10 and 15 km depth to estimate the sentivity of the solution along strike.

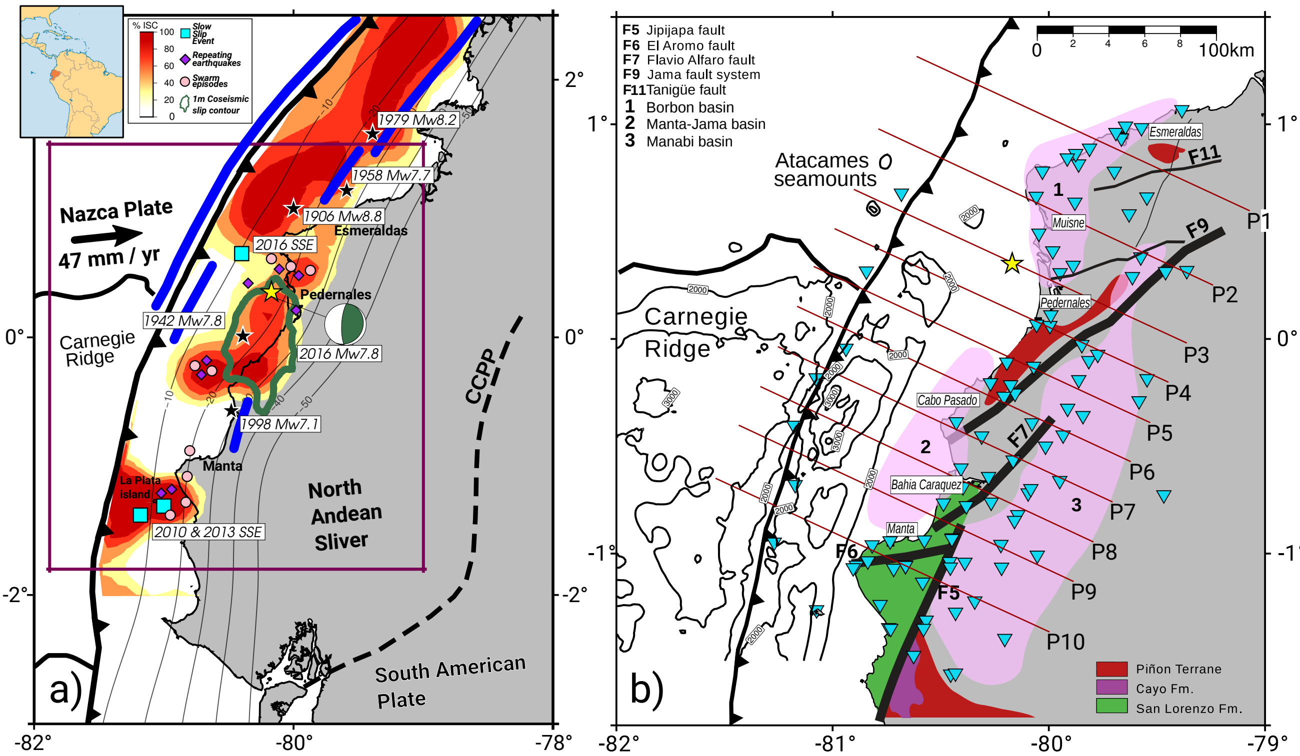

Figure 1: **Seismotectonic and geological setting. a)** Seismotectonic setting of the study area. Solid blue lines represent the extension of historical earthquakes in the area. Epicentres of those events are indicated with a black star. Slow slip events, repeating earthquakes and seismic swarm episodes are also represented by squares, diamonds and circles, respectively. 2016 Pedernales earthquake is shown including its epicentre (yellow star), cosesimic slip by Nocquet et al., 2017 (solid green line) and focal mechanism (green beach ball). Distribution of the interseismic coupling by Nocquet et al. (2014). Chingual-Cosanga-Pallatanga-Puna fault (CCPP) that created the North Andean Sliver (NAS) is represented by a segmented line. **b)** Geological context and recording network. Main formations, sedimentary basins and faults mapped by Reyes and Michaud (2012) are displayed by coloring forms and solid black lines. Offshore, residual bathymetry derived by Agurto-Detzel et al. (2019) is shown in solid black line. Permanent Ecuadorian network (RENSIG, Alvarado et al., 2018) and emergency deployment (Meltzer et al., 2019) are shown in gray inverted triangles. Profiles, P1-P10, discussed in this work are plotted in solid red line. Yellow star represents the epicentre of the 2016 Pedernales earthquake (Nocquet et al., 2017).

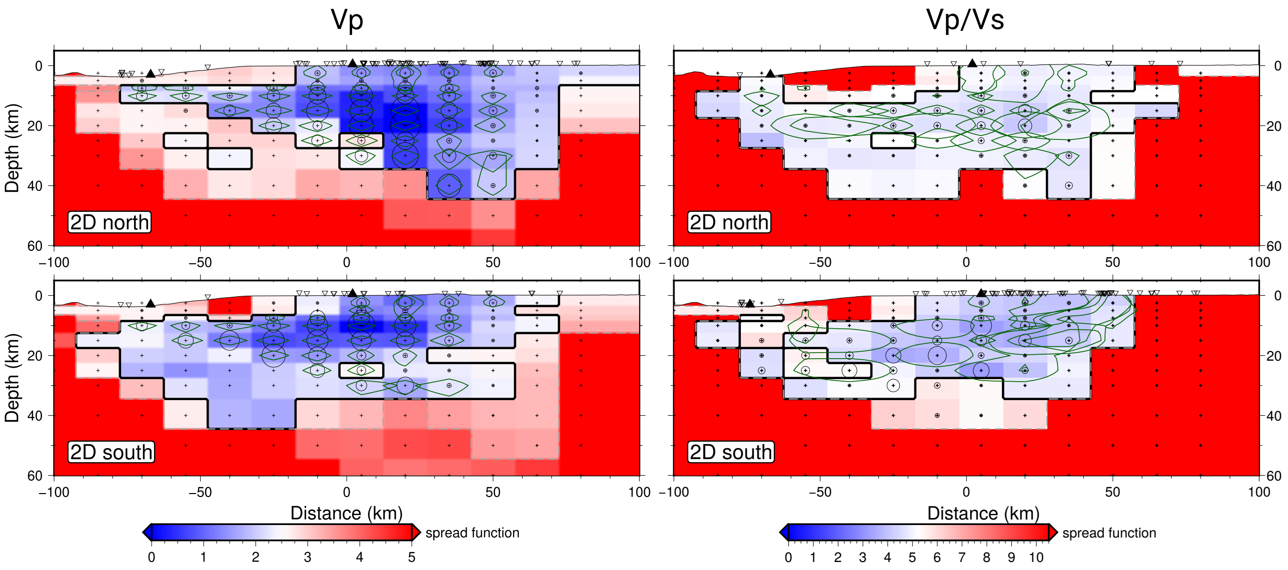

Figure 2: **2D model resolution matrix (MRM).** Resolution contour estimation for the 2D Vp and Vp/Vs models in the north and south segments. Based on the MRM analysis, calculation of the spread function is dipslayed in a red/blue scale. Green lines show the 70% contour for the diagonal elements of the MRM.

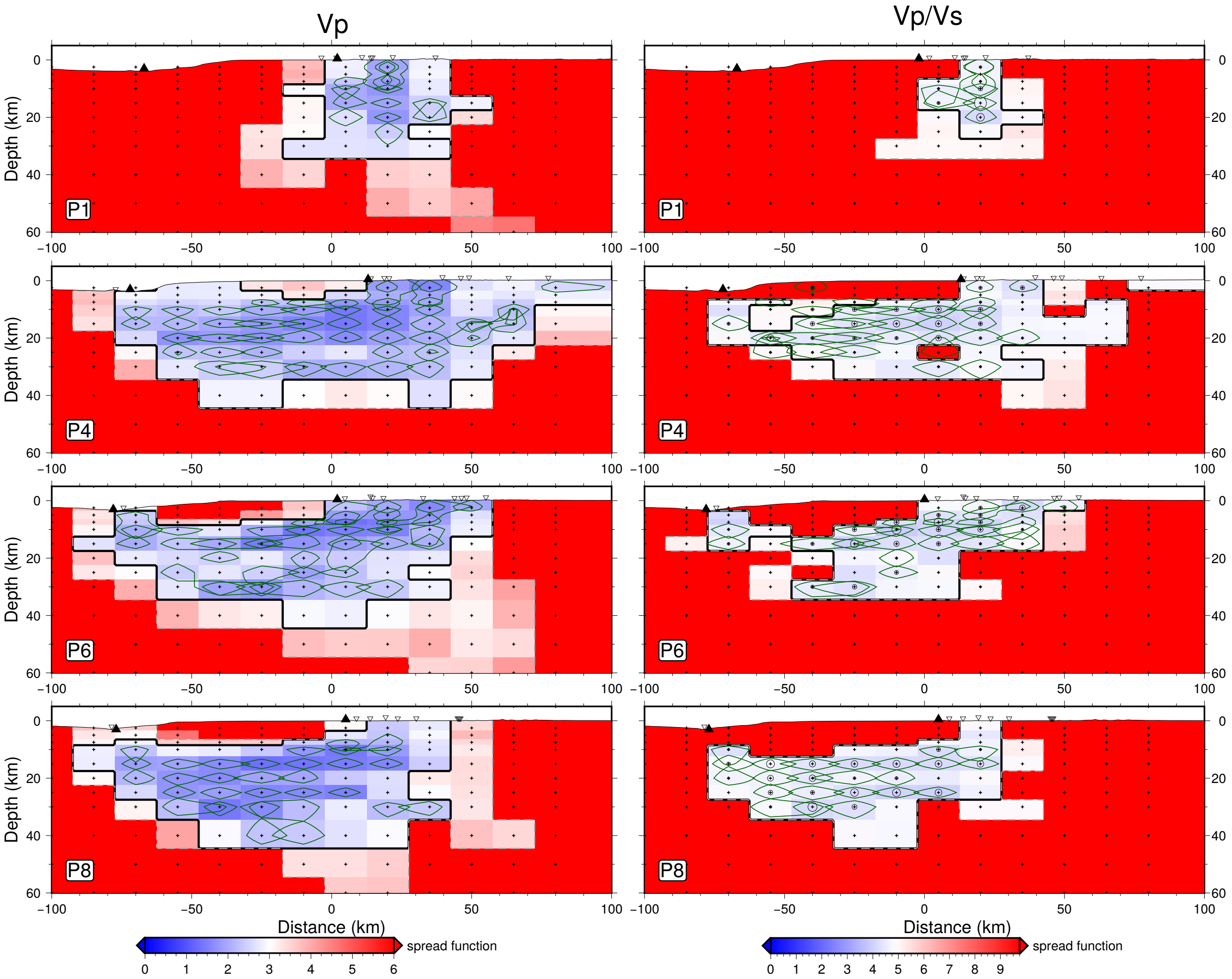

Figure 3: 3D model resolution matrix (MRM). Resolution contour estimation for the 3D Vp and Vp/Vs along representative profiles for the northern, central and southern parts of the area of study. Based on the MRM analysis, calculation of the spread function is shown by a red/blue scale. Green lines show the 70% contour for the diagonal elements of the MRM. See text for further information.

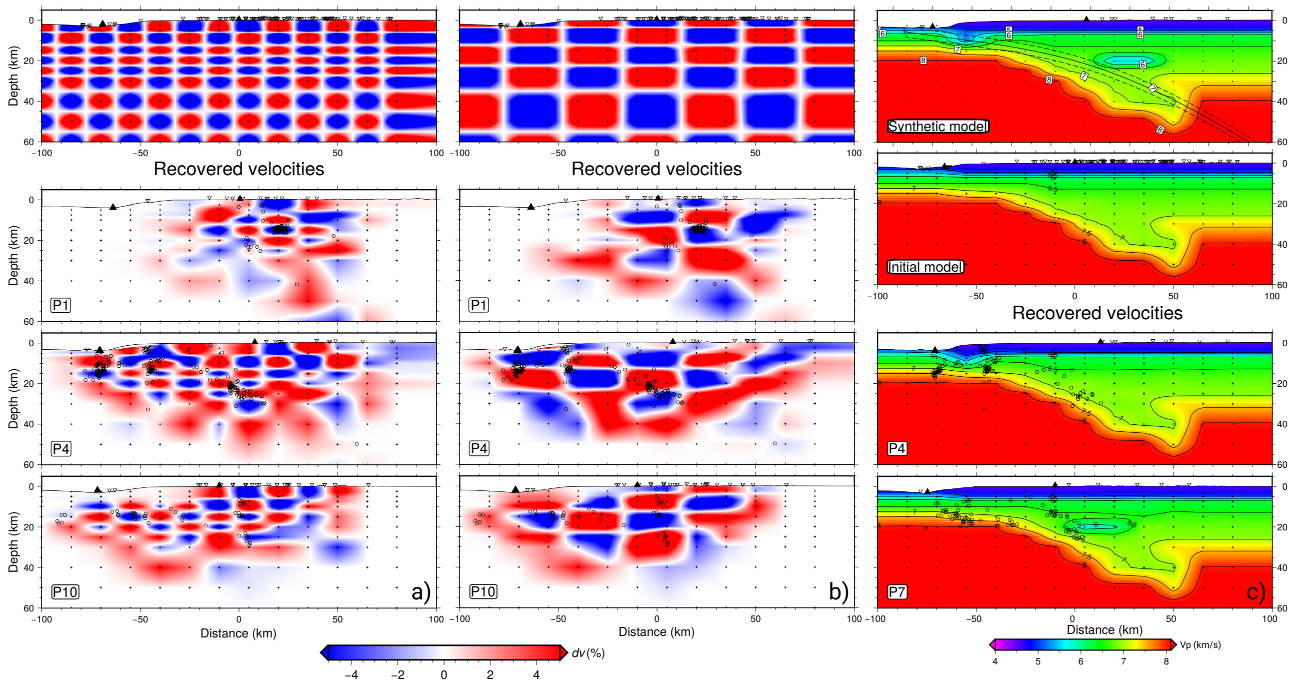

Figure 4: **Synthetic recovery tests.** Checkerboard test for **a)** small, 15km and **b)** medium, 30 km anomalies. Top image show the input model comprised by alternated positive and negative anomalies of ±5% of the inverted model. Bottom images show the recovered velocities along representative profiles for the northern, central and southern segments in our region of interest. **c)** Restoring test for a seamount represented by low Vp (5.0 km/s) anomalies added in P4 and a low velocity anomaly (5.5 km/s) at 20 km depth in P7. Projection of the synthetic and initial model are shown at the top. See Figure S4 and S5 for furhter details.

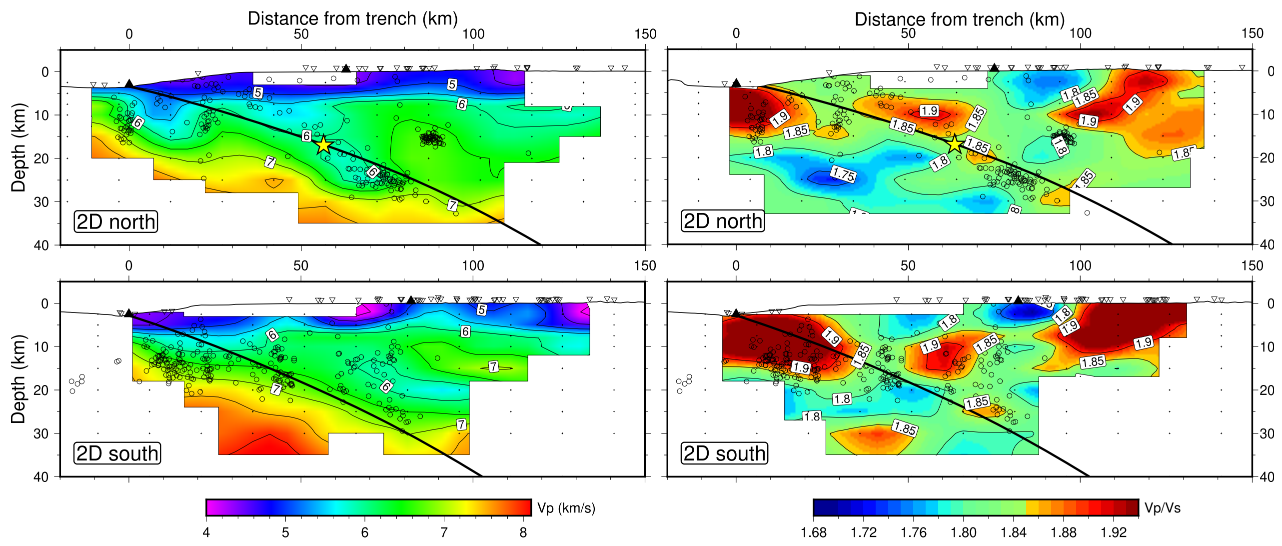

Figure 5: **2D velocity model.** Two-dimensional models for both north (top) and south (bottom), Vp (left) and Vp/Vs (right). Velocities and Vp/Vs ratios are color coded and iso-contours are plotted every 1.0 km/s and 0.025 for Vp and Vp/Vs, respectively. Based on resolution estimated by the MRM and checkerboard test, results for non resolved areas are shown faded or blank. Relocated hypocenters are plotted in black circles and grid nodes are shown in black crosses. Yellow star in north, Vp and Vp/Vs, profiles indicates the epicenter for the 2016 Pedernales earthquake (Nocquet et al., 2017). Solid black triangles represent the projection of the trench (Collot et al., 2005) and coastline. Modified slab interface (see text for further details) is represented by solid black line. Finally, inverted triangles are the stations contained on each profile.

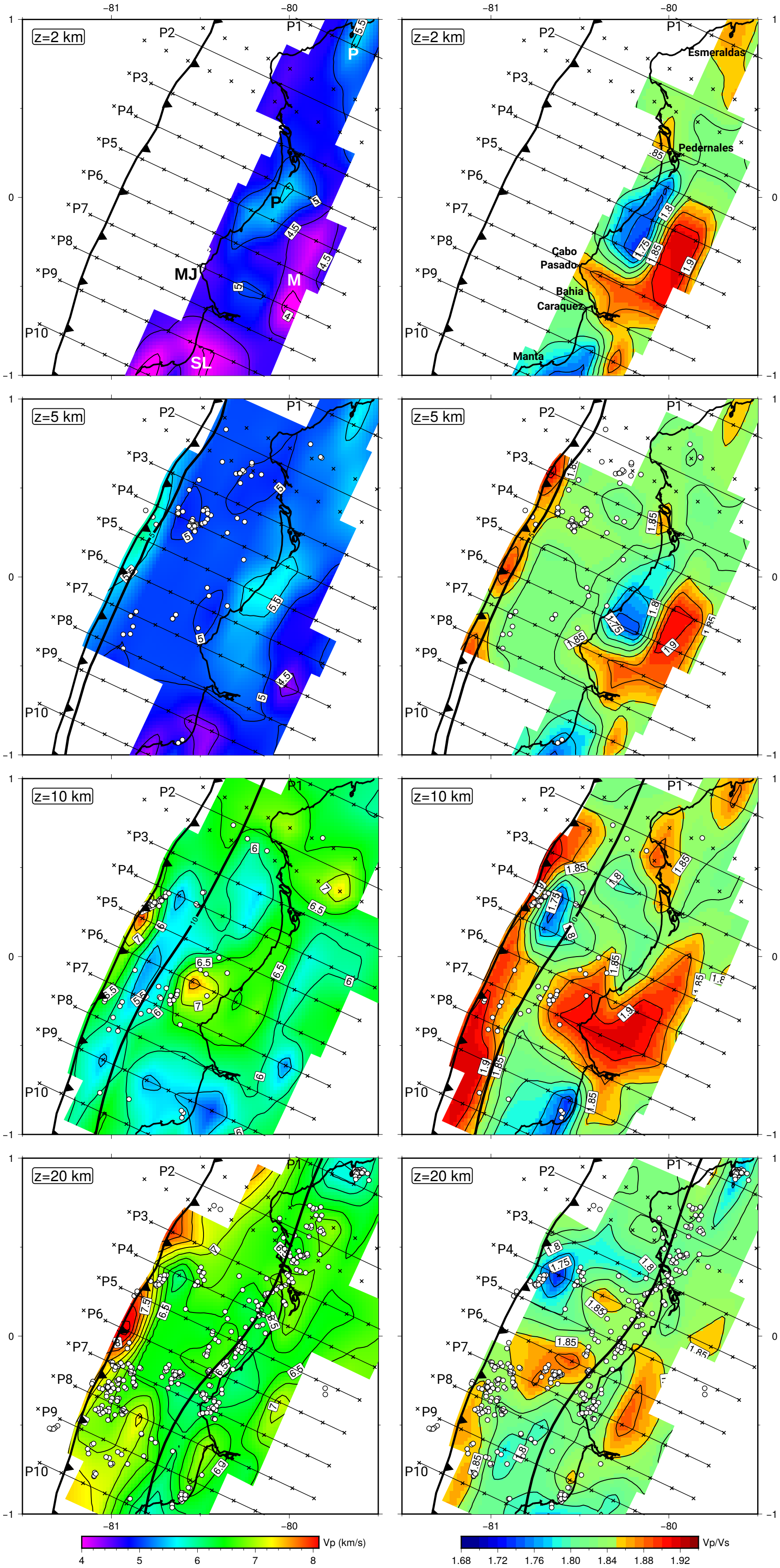

Figure 6: **3D velocity model, horizontal slices.** Vp (left) and Vp/Vs (right) horizontal slices at 2, 5, 10 and 20 km depth. Velocities and Vp/Vs ratios are color coded and iso-contours are plotted every 1.0 km/s and 0.025 for Vp and Vp/Vs, respectively. Based on MRM and checkerboard test, non resolved areas are blank. Velocity anomalies colocated to surface observations from Reyes and Michaud (2012) and cities referred in text are shown in z=2 km. Profile and grid nodes locations are displayed by black solid line and crosses, respectively. Corresponding slab depth contour is represented by a thick black line. Seismicity is plotted by depth (d) following: d≤5 km in z=5 km, 5<d≤10 km in z=10 km and d>10 km in z=20 km. P: Piñon outcrop, M: Manabi basin, MJ: Manta-Jama basin and SL: San Lorenzo block.

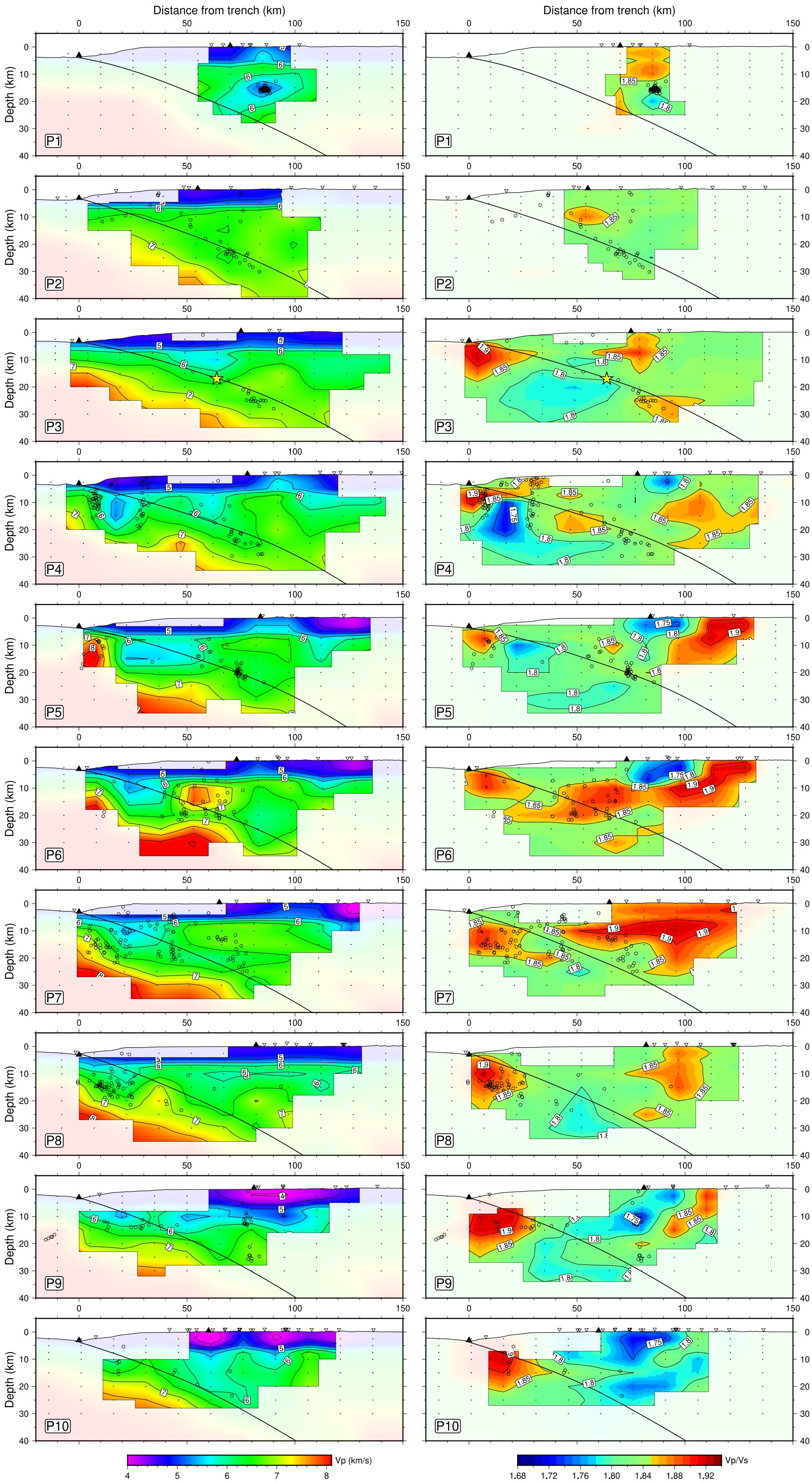

Figure 7: **3D velocity model, cross sections** Three-dimensional models for both Vp (left) and Vp/Vs (right) based on the inversion of a smooth initial 2D initial model and 2D-N and 2D-S arrival times. Results are shown along 10 W-E profiles. Vp velocities and Vp/Vs ratios are color coded and iso-contours are plotted every 1.0 km/s and 0.025 for Vp and Vp/Vs, respectively. Based on the MRM and checkerboard test, non resolved areas are faded. Location of profiles, P1-P10, is shown in Figure 1. Width for projection of hypocenters and stations is 22 km. Relocated hypocenters are plotted in black circles, and stations are represented by inverted triangles. Grid nodes are displayed in black crosses and solid black triangles represent the projection of the trench and coastline. Yellow star in P3 indicates the hypocenter for the 2016 Pedernales earthquake (Nocquet et al., 2017). Modified slab interface (see text for further details) is represented by solid black line.

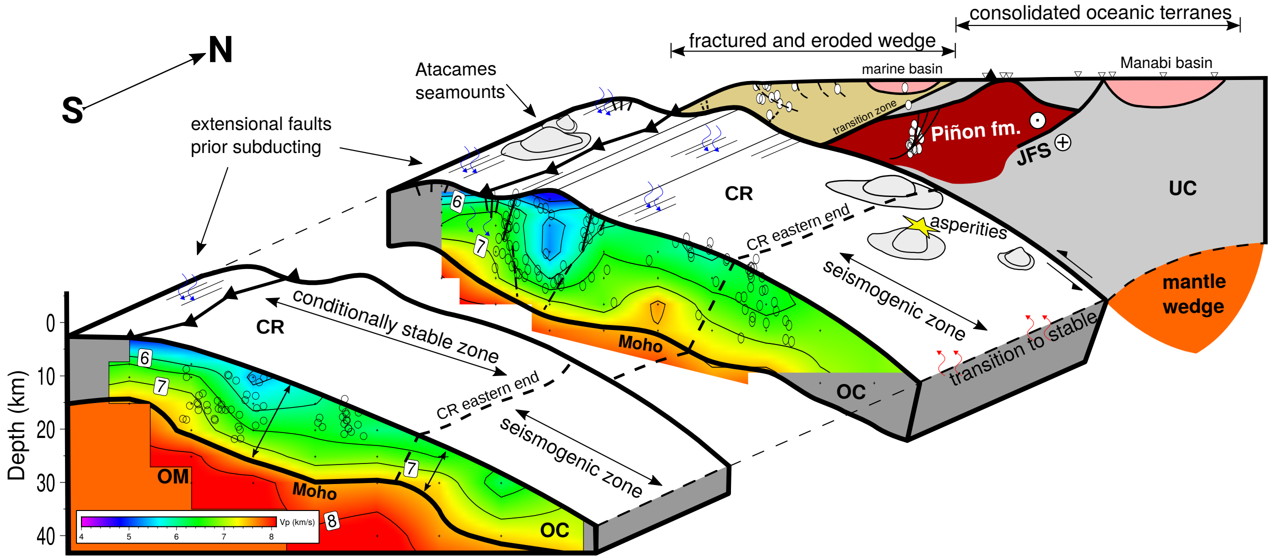

Figure 8: **Interpretative sketch.** Structural synthesis based on the main findings of this work around profile P4 and P7. UC: upper plate crust, OC: oceanic crust, OM: oceanic mantle, CR: Carnegie Ridge, JFS: Jama fault system, with strike-slip displacement indicated by the dot and cross. Vp velocities at P4 and P7 are projected in cross sections. Hypocenters are shown in circles. Black triangles represent the trench axis and the coastline. Inverted triangles indicate station locations. Yellow star represents the epicentre of the 2016 Pedernales earthquake (Nocquet et al., 2017). Arrows in the front panel indicate the thickness of the OC. We observe a thinning of the OC at depths ∼20-30 km which we interpret as the eastern end of the CR. Vertical scale exaggeration 1:1.5.